



A numerical investigation into gas production under worst case scenario of limited heat transfer

Shadman Hasan Khan^{1,4} · A. Kumari^{1,4} · G. Dixit² · C. B. Majumder^{1,4} · A. Arora³

Received: 14 July 2020 / Accepted: 27 June 2021 / Published online: 6 July 2021
© The Author(s), under exclusive licence to Springer Nature B.V. 2021

Abstract

Depressurization technique is considered as one of the most promising techniques in dissociating gas hydrates. However, since dissociation of hydrates is an endothermic process. Dissociation alone through depressurization is not a feasible technique due to limited heat transfer. The reduced heat transfer results in rapid cooling, thereby causing reduced permeability due to ice formation and re-formation of hydrates. The objective of the current study is to investigate the viability of depressurization under worst case scenario of suppressed heat transfer. The worst case scenario is simulated by employing Newman boundary of no heat flux from the surroundings. The novelty of the present work lies in investigating the gas production behavior using depressurization in a worst case scenario. For this purpose, a 2D model is applied for a 150 m × 150 m system. A production well is placed at the center of the domain. The depressurization is performed by the withdrawal of fluids from the production well. In order to determine the suitable depressurization rate, the withdrawal of fluids is carried out within a range of 0.01–0.6 kg/s. The overall cumulative production at the well (mass of CH₄) is determined. In this study, we demonstrate that three major causes, namely ice formation, secondary hydrates and reservoir achieving steady state are responsible for stopping of gas production. Insights into the dissociation behavior of the cases analysed are obtained from the contours of gas, water, hydrate, pressure, equilibrium pressure, temperature, relative gas permeability, and relative water permeability.

Keywords Energy · Depressurization · Methane hydrate · Simulation · Efficiency

List of symbols

b	Slippage factor
c _R	Specific heat capacity of rock [J/(kg K)]
E _a	Activation energy (J/mol)
F _A	Area adjustment factor
f _{eq}	Equilibrium fugacity of gas phase
f _g	Fugacity of gas phase
g	Gravitational acceleration (m/s ²)
G	Gas phase denotation
H	Height of hydrate reservoir (m)
H _{dep}	Specific enthalpy of departure of gas (J/kg)

H _m	Specific enthalpy of methane in water (J/kg)
H _{isol}	Specific enthalpy corresponding to inhibitor dissolution in water (J/kg)
H _{msol}	Specific enthalpy corresponding to methane dissolution in water (J/kg)
h _{mG}	Specific enthalpy of methane in gas (J/kg)
h _w	Specific enthalpy of water in water (J/kg)
K _{Aq}	Thermal conductivity of water [W/(m K)]
K _G	Thermal conductivity of gas [W/(m K)]
K _H	Thermal conductivity of hydrate [W/(m K)]
K _I	Thermal conductivity of ice [W/(m K)]
K _R	Thermal conductivity of rock [W/(m K)]
K _{id}	Absorption distribution coefficient (m ³ /kg)
k _{d0}	Intrinsic reaction rate of hydrate [mol/(m ² Pa s)]
k	Intrinsic permeability (m ²)
k _{rAq}	Relative permeability of water
k _{rg}	Relative permeability of gas
L	Hydrate reservoir length (m)
M _m	Molecular weight of CH ₄ (g/mol)
M _w	Molecular weight of H ₂ O (g/mol)
N	Hydration number (6)
P _{Aq}	Pressure exerted by water phase (Pa)

✉ Shadman Hasan Khan
skhan1@ch.iitr.ac.in

¹ Indian Institute of Technology, Roorkee, Roorkee 247667, India

² Gas Hydrate Research & Technology Centre, Panvel, Mumbai, Maharashtra 410106, India

³ Shaheed Bhagat Singh State Technical Campus, Ferozpur, Punjab 152004, India

⁴ Department of Chemical Engineering, IIT Roorkee, Roorkee, India

P_{eq}	Equilibrium pressure of hydrate (Pa)
P_G	Pressure exerted by gas phase (Pa)
q_d	Heat injection rate (W)
q_I	Water injection rate of water (m^3/s)
R	Gas constant
S_W	Saturation of water (fraction)
S_G	Saturation of gas (fraction)
S_H	Saturation of hydrate (fraction)
S_{ICE}	Saturation of ice (fraction)
T	Temperature of reservoir ($^{\circ}C$)
t	Time (s)
U_{dep}	Specific internal energy of departing gas mixture (J/kg)
u_{mG}	Specific internal energy of CH_4 in gas phase (J/kg)
u_{wG}	Specific internal energy of H_2O in gas phase (J/kg)
u_H	Specific internal energy of gas hydrate (J/kg)
u_I	Specific internal energy of ice (J/kg)
u_m	Specific internal energy of CH_4 in water phase (J/kg)
MHSZ	Methane hydrate stability zone
BHSZ	Bottom of hydrate stability zone

Introduction

Gas hydrates are ice-like crystalline compounds formed under specific thermodynamic conditions via inclusion of gas and water molecules (Sloan and Koh 2007; Arora and Cameotra 2014). The formation occurs by the encapsulation of natural gas molecules by physical or chemical bonds inside the polyhedral cages of water molecules (Tang et al. 2007; Gupta et al. 2009; Arora and Singh 2015; Fang et al. 2019). Hydrates are stable at high pressure and low-temperature conditions, and any changes from this stability lead to gas hydrate dissociation (Li et al. 2012a). One cubic meter hydrate contains approximately $164 m^3$ of methane gas at standard temperature and pressure (Zhou et al. 2014). Hydrates are known to occur in different hydro-geologic settings, such as the permafrost regions, deep ocean sediments, and submarine continental slope sediments across the west coast of Africa, US Atlantic continental slope, Mackenzie Delta, Blake Ridge and British Columbia (Waite et al. 2020). Other reported sites include northern California (Field 1990), Alaskan Beaufort Sea Continental margin (Nixon and Hayley 2011), and offshore Norway (Bourriak et al. 2000). Gas hydrates can provide at least twice as much energy compared to all other resources of fossil fuels (Terzariol et al. 2017; Li et al. 2018). The amount of carbon in the natural gas hydrate is twice the amount of carbon in all other fossil fuels (Feng et al. 2015). The global reserves for methane from oceanic hydrate reserves are estimated

as $1-5 \times 10^{15} m^3$ (Konno et al. 2010). Gas hydrate reserve estimations for the Ulleung basin, Japan, are estimated to be $8.43 \times 10^8 m^3$ (Yi et al. 2018). Canada gas hydrate reserves are estimated as $0.19-6.2 \times 10^{14} m^3$ in the Arctic Archipelago, $0.24-8.7 \times 10^{13} m^3$ in the Mackenzie delta-Beaufort Sea, $0.32-2.4 \times 10^{13} m^3$ on the Pacific margin, and $1.9-7.8 \times 10^{13} m^3$ on the Atlantic margin (Majorowicz and Osadetz 2001). The US gas hydrate reserves (recoverable) are estimated as $1.9 \times 10^{14} m^3$ in the Gulf of Mexico (offshore) and $4.4 \times 10^{14} m^3$ along Eastern US (offshore) (Collett 1995).

There are four main classes of methane hydrate deposits such as Class 1 (North Slope of Alaska), Class 2 (Nankai Trough), Class 3 (Qilian Mountain Permafrost in China), and Class 4 (Krishna Godavari Basin in India) (Gao et al. 2018; Lu et al. 2018). Class 1 hydrate accumulations have two distinct zones: an upper hydrate-bearing interval which has low effective permeability, and an underlying two-phase zone (free gas + water) (Moridis and Sloan 2007; Lee et al. 2011). Class 2 hydrate deposits comprise of 2 zones: an upper hydrate-bearing layer and an underlying aquifer (only water without free gas) (Moridis and Sloan 2007; Cui et al. 2018). Class 3 accumulations consist of only a single zone, a hydrate-bearing layer without any underlying zone (Moridis and Sloan 2007; Lee et al. 2011). Class 4 hydrates are characterized by low saturation ($Sh < 0.1$) dispersed hydrates without any confining layers (Moridis and Sloan 2007; Cui et al. 2018). The viability of gas production from Class 2 and 3 reservoirs requires consideration of thermodynamic, environmental, and economic factors. Moreover, the energy extraction from the different hydrate reservoir types demands accurate quantitative estimation as well as characterization (Wang et al. 2018) of several parameters. These parameters include media properties (porosity and intrinsic permeability), wettability properties (relative permeability and capillary pressure), thermal properties (specific heat and thermal conductivity) and geomechanical properties (Poisson's ratio, cohesion, Young and shear moduli (Moridis et al. 2019). Recent studies conducted by Jin et al. (2020) employed seismic data to understand migration of fluids to gas hydrate stability zone (GHSZ). Various models for hydrate formation and estimation have been proposed in the literature. A formation model for low concentration disseminated hydrates considering local biogenesis, with a CH_4 source within Methane hydrate stability zone (MHSZ), assuming no transport or diffusion was proposed by Davie and Buffett (2001, 2003a, b). Formation models for fracture filling hydrates, with CH_4 source within MHSZ, considering local diffusion as a dissolved phase were proposed by Malinverno (2010), Malinverno and Goldberg (2015) and Nole et al. (2017). A more specific model applicable to disseminated hydrates and enriched hydrates at bottom stability was proposed by Frederick and Buffett (2011), Nole

et al. (2016) and VanderBeek and Rempel (2018). The CH₄ source is considered below the bottom of hydrate stability zone (BHSZ) with dominant transport mechanism as advection. Burwicz et al. (2011) and Nole et al. (2018) proposed a model for methane recycling considering methane source near and below BHSZ considering free gas flow as the dominant transport mechanism. A more generalized model applicable to different hydrate deposits namely, enriched hydrates near BHSZ, vent side, concentrated hydrates, was presented by You et al. (2015) and You and Flemings (2018). Moreover, a mechanistic model explaining the solidification of gas hydrate reservoirs was developed by Behseresht and Bryant (2012). The application of spectral decomposition technique was demonstrated by Oliveira et al. (2010). Their research yielded a better understanding of the gas hydrate deep water system located in Pelotas basin off the Brazilian coast. Excellent incorporation of existing technologies for gas hydrate exploration was performed by Shelander et al. (2010). Their implementation utilizes pre-stack seismic inversion data, elastic properties modeling, and seismic interpretation to predict gas hydrate saturation (Sh). The foundation of numerical simulations is often built upon the accuracy of such estimates and calculated thermophysical properties (Goto et al. 2017). Recent numerical studies conducted by Riley et al. (2019) highlighted the importance of heterogeneities in saturation estimation, which can affect gas production rate by up to 40%. A far more robust thermo-hydro-mechanical formulation using the code-bright simulator was validated against the international code comparison study (Wilder et al. 2008) by De La Fuente et al. (2019). The energy extraction from hydrate reservoirs is dictated through the long term viable production potential as well as the social, environmental, and economic considerations. The dissociation of offshore hydrates (both present scenario and future dissociation) as a result of ocean warming and its dynamic response was investigated by Marín-Moreno (2014), over a 2300 years period. An excellent starting point for assessing gas hydrate exploitation projects by considering social, economic and environmental consequences via a multi-criteria decision analysis (MCDA) protocol was proposed by Riley et al. (2020).

Natural gas can be produced from hydrates by three methods such as depressurization, thermal stimulation (Singh et al. 2015), chemical or inhibitor injection, and any combination of these three production methods (Moridis and Reagan 2007; Xu et al. 2018). The depressurization method is the most economical method for gas production from gas hydrates because there is no need to supply the external source of energy during gas production (Yu et al. 2019). However, sustaining continuous production using depressurization requires resolving problems such as secondary hydrate formation (Li et al. 2011; Su et al. 2012), meta-stability issues (Sun et al. 2019), sand generation

(Yuan et al. 2017; Yan et al. 2018), bottom floor subsidence and well stability issues (Wan et al. 2018). Over the years, various depressurization approach like multiple wells (Li et al. 2013; Yu et al. 2020), horizontal wells (Li et al. 2012b, 2013), vertical wells (Liang et al. 2018), and cyclic depressurization (Konno et al. 2016) have been investigated. Several studies have reported the consequences of different depressurization approaches like rapid depressurization, stage-wise depressurization, along with hybrid dissociation techniques. Sun et al. (2019) investigated the metastability of hydrates in super-cooled water environment induced by depressurization. Gao et al. (2018) demonstrated that in case of water excess deposits, Class 3 show better production characteristics than class 2 deposits using depressurization. Chong et al. (2017) concluded that depressurization results in a faster initial production along with rapid temperature drop in comparison to thermal stimulation. Heeschen et al. (2016) conducted experimental studies using (LARS; 210 L) and concluded that data for low and moderate gas production rates showed agreement with the Mallik drill site, while it was different at higher production rates. Circone et al. (2000) reported anomalous preservation of hydrate under rapid depressurization conditions. Yang et al. (2012) concluded that the rate of gas production in different dissociation stages by the depressurization method is not uniform. Yu et al. (2019) simulated Nankai Trough to investigate gas recovery enhancement from the hydrate reservoir using single and double vertical well. Ruan et al. (2012) showed that the final gas production could be significantly affected by the depressurization range. When it comes to understanding the mechanisms, an extensive discussion regarding the causes of hydrate formation, gas migration, gas pockets, and dissociation can be found here (Crutchley et al. 2010a, b, 2014; Chen et al. 2014; Yang et al. 2015; Hillman et al. 2020; Khan et al. 2020).

The present study aims at demonstrating the need to establish the response to the depressurization process under conditions of limited heat flux from surroundings. The novelty of the present work lies in investigating gas production behavior from hydrate reservoirs under worst case scenario of limited heat transfer from the boundaries. To our knowledge, none of the published depressurization studies focus on establishing the course of hydrate dissociation behavior through depressurization under limited conditions of heat transfer. As such, depending upon the phase saturations of the system, lithological parameters and thermodynamic parameters, namely initial pressure and temperature, a suitable depressurization range exists, which leads to maximum gas production. However, some systems are more sensitive towards changing magnitude of depressurization. In the present study, a coupled Thermo-Hydro implementation using Tough+Hydrate is used to simulate five different scenarios of hydrate-bearing media, with different phase

saturation of gas, hydrate, and water. Initially, the system is assumed to be at equilibrium, and three phases are present. The system is depressurized with a single well placed at the center of the domain. The depressurization is conducted for different magnitude with withdrawal rates in the range of 0.01–0.6 kg/s. From the results, the different causes of seizing of gas production from the well, sensitivity of the system towards depressurization, and quantitative analysis are carried out.

Numerical modeling approach

Assumptions

Some of the assumptions in this study are mentioned below.

- Darcy’s law is considered to be valid within the conditions studied.
- The relative magnitude of dispersion is small in comparison to advection.
- The geologic medium movement owing to freezing is not described. A high pore compressibility is used to account for density differences between ice and aqueous phases.
- During freezing, dissolved salts do not precipitate, although their concentration increases.
- The effect of diffusion is neglected in mass transportation.

Equilibrium model equations

Here, Tough + hydrate (T + H) has been applied for numerical modeling of the conceptualized hydrate reservoir. T + H has been developed by Lawrence Berkeley national laboratory, USA (Moridis et al. 2005) and is capable of modeling up to four mass components (water, CH₄, hydrate, and water-soluble inhibitors), which are partitioned among four possible phases (gas, liquid, ice, and hydrate). Tough + hydrate has been widely used for numerical modeling of both field-scale and lab-scale experiments. (Tang et al. 2007; Seol and Myshakin 2011; Birkedal et al. 2014). The equilibrium model of hydrate dissociation is used in the current study. The choice between equilibrium and kinetic models depends upon both spatial scale (Tang et al. 2007) and time scale (Teng and Zhang 2020) associated with the problem. The kinetic model is a more generalized model that simplifies into equilibrium model when time scales of hydration reaction are smaller than that of physical processes such as convective and diffusive transport of heat and mass. Kowalsky and Moridis (2007) suggested that equilibrium reaction model is a feasible choice for field-scale production simulations, while kinetic considerations are essential for lab-scale modeling (Tang et al. 2007; Feng et al. 2019). The summary of conservations equations (Moridis et al. 2012; Yin et al. 2016) used in the equilibrium model in Tough + Hydrate is described in Table 1 as follows:

The complete form of the general equations in Table 1 are represented in Eqs. 1–4

1. Mass balance Equation for Methane (CH₄)

$$\frac{\partial}{\partial t} (\phi S_{Aq} \rho_{Aq} x_{Aq}^m + \phi S_G \rho_G x_G^m + \frac{M^m}{M^h} \phi S_H \rho_H) = \nabla \cdot \left[-k \frac{k_{rAq} \rho_{Aq}}{\mu_{Aq}} x_{Aq}^m (\nabla P_{Aq} - \rho_{Aq} g) - k \left(1 + \frac{b}{P_G} \right) \frac{k_{rG} \rho_G}{\mu_G} x_G^m (\nabla P_G - \rho_G g) \right] + q_{Aq} x_{Aq}^m + q_G x_G^m \quad (1)$$

2. Mass balance equation for Water (H₂O)

$$\frac{\partial}{\partial t} (\phi S_{Aq} \rho_{Aq} x_{Aq}^w + \phi S_G \rho_G x_G^w + \phi S_I \rho_I + \frac{NM^w}{M^h} \phi S_H \rho_H) = \nabla \cdot \left[-k \frac{k_{rAq} \rho_{Aq}}{\mu_{Aq}} x_{Aq}^w (\nabla P_{Aq} - \rho_{Aq} g) - k \left(1 + \frac{b}{P_G} \right) \frac{k_{rG} \rho_G}{\mu_G} x_G^w (\nabla P_G - \rho_G g) \right] + q_{Aq} x_{Aq}^w + q_G x_G^w + \frac{q_I \rho_{Aq}}{LWH} \quad (2)$$

Table 1 The first two represents mass conservation and third row represents energy conservation equation

Accumulation terms	Flux terms	Sink/source term
$\frac{d}{dt} \int_{V_n} M^k dV =$ $M^k = \sum_{\beta=Aq,G,H,I} \phi S_{\beta} \rho_{\beta} X_{\beta}^k$	$\int_{V_n} F^k \cdot n d\Gamma +$ $F^k = \sum_{\beta=Aq,G} F_{\beta}^k$	$\int_{V_n} q^k dV$ $\hat{q}^k = \sum_{\beta=Aq,G} X_{\beta}^k q_{\beta}$
$M^{\theta} = (1 - \phi) \rho_R C_R T + \sum_{\beta=Aq,G,I} \phi S_{\beta} \rho_{\beta} X_{\beta}^K + \Delta(S_H \rho_H U_H^{\theta}) - [(1 - \phi) K_R + \phi (\sum_{\beta=Aq,G,H,I} \phi S_{\beta} K_{\beta})] \nabla T + \sum_{\beta=Aq,G} H_{\beta} F_{\beta} + \sum_{\beta=Aq,G} \phi S_{\beta} \sigma_{\beta} \nabla T_d + \sum_{\beta=Aq,G} X_{\beta}^K q_{\beta}$		

Here, V , V_n denote volume, volume of subdomain n , M^k represents the mass accumulation term of component (κ), A , Γ_n denote the surface area, surface area of subdomain n , F^k is the Darcy flux vector of component κ , n is the inward unit normal vector, q^k represent source/sink term of component κ , ϕ is porosity, ρ_{β} is the density of phase β , ρ_R denotes rock density, C_R is the heat capacity of the dry rock, Q_{diss} is hydrate dissociation heat, S_{β} represents saturation of phase β , U_{β} is the specific internal energy of phase, X_{β}^k denotes mass fraction of component κ in phase β

3. Mass balance equation for inhibitor

for suppressed heat transfer across the boundaries. Hence, the

$$\frac{\partial}{\partial t} \left\{ [\varphi S_{Aq} + (1 - \varphi) \rho_R K_d^i] \rho_{Aq} x_{Aq}^i \right\} = \nabla \cdot \left[-k \frac{k_{rAq} \rho_{Aq}}{\mu_{Aq}} x_{Aq}^i (\nabla P_{Aq} - \rho_{Aq} g) \right] + q_{Aq} x_{Aq}^i \tag{3}$$

4. Energy Balance Equation

flux along the top and bottom boundaries of the hydrate-bearing layer is assumed to be zero. To realize such boundaries

$$\begin{aligned} \frac{\partial}{\partial t} \left\{ (1 - \varphi) \rho_R C_R T + \varphi S_{Aq} \rho_{Aq} \left[x_{Aq}^w u^w + x_{Aq}^m (u^m + u_{sol}^m) + x_{Aq}^i u_{sol}^i \right] + \varphi S_G \rho_G (x_G^w U_G^w + x_G^m U_G^m + U_{dep}) \right\} \\ + \varphi S_I \rho_I u_I + \varphi S_H \rho_H u_H + \varphi \Delta S_H \rho_H \Delta H^0 + \varphi \Delta S_I \rho_I \Delta H^f \\ = \nabla \cdot \{ [(1 - \varphi) K_R + \varphi S_H K_H + \varphi S_I K_I + \varphi S_{Aq} K_{Aq} + \varphi S_G K_G] \Delta T \} \\ + \nabla \cdot \left[k \left(1 + \frac{b}{P_G} \right) \frac{k_{rG} \rho_G}{\mu_G} (\nabla P_G - \rho_G g) (x_G^w h_G^w + x_G^m h_G^m + H_{dep}) + k \frac{k_{rAq} \rho_{Aq}}{\mu_{Aq}} (\nabla P_{Aq} - \rho_{Aq} g) (x_{Aq}^w h^w + x_{Aq}^m (H^m + H_{sol}^m) + x_{Aq}^i H_{sol}^i) \right] \\ + \frac{q_I \rho_{Aq} h^w}{LWH} + \frac{q_d}{LWH} + \left\{ q_G [x_G^w h_G^w + x_G^m h_G^m + H_{dep}] + q_{Aq} [x_{Aq}^w h^w + x_{Aq}^m (H^m + H_{sol}^m) + x_{Aq}^i H_{sol}^i] \right\}. \end{aligned} \tag{4}$$

Geometry, domain discretization, and system properties

The dimensions of the model domain are 150 m × 150 m × 10 m. The production well is placed at the center of the domain. Since the system is homogenous, taking advantage of the symmetry, only a quarter of the system is simulated to save computational effort and time. The system is described as a 2D rectangular coordinate system to simulate the dissociation behavior of methane hydrate.

The Cartesian model is discretized into a total of 5724 elements along the X–Y axis. The depth of domain is considered along the Z direction, and only a single cell is kept to model the system as 2D. The physical properties and initial conditions of the numerical model, as shown in Table 2, are representative of marine hydrate reservoir sites discovered during the National Gas Hydrate Program (NGHP-01) in India (Collett et al. 2015). Several gas hydrate sites discovered in the Krishna Godavari basin (Collett et al. 2015) have been identified with thin confining strata, while some sites are classified as unconfined hydrate deposits (Collett et al. 2015). Studies conducted by Phirani et al. (2009) concluded that external heat transfer, i.e., thermal stimulation is necessary to sustain dissociation in unconfined hydrate deposits. The enthalpy of dissociation comes from the porous medium, over-burden, and under-burden (Bhade and Phirani 2015; Song et al. 2015). Hence, dissociation depends on available enthalpy within the hydrate reservoir (Bhade and Phirani 2015). Therefore, a thin layer/absence of sediment implies limited potential of heat supply from surroundings. However, it must be noted that complete suppression of heat transfer from surroundings should be considered as the “worst possible condition” for gas production. The present study is designed with an aim to investigate the worst-case scenario

conditions physically, Neumann B.C. is used for the top and bottom boundaries. Figure 1a illustrates the overall numerical representation of the system and Fig. 1b depicts the pertinent boundary conditions applied to the quarter of the domain.

Grid independence test

Before beginning any rigorous computational study, a suitable grid with appropriate discretization must be selected. The criterion for grid selection includes (i) Repetition and reproducibility of results (ii) Feasible computational requirements. The reproducibility and repetition are tested by using a certain “Quantifiable” parameter. For present studies, “mass of CH₄ (kg)” (both Net production and from hydrate) is determined and plotted for the different grid index. In the present study, six different grid sizes were used to test grid convergence. The details of the different discretization employed during the Grid independence test are described in Table 3. The grid can be classified as coarse, medium, and Fine based on the number of mesh elements. The fine Grid consists of 25,699 elements (Grid V), while the coarse Grid consists of 1699 elements (Grid 0). The plot of methane mass (kg) for the different grid index is shown in Fig. 2. The numerical prediction from the Grid V (finest) is considered to be the benchmark, i.e., standard for testing accuracy of other coarser Grids. The absolute error (ε) in prediction is calculated using the following mathematical formulation.

$$\epsilon = \frac{|M_V - M_i|}{M_V} \times 100$$

where, ε represents an absolute error, M_V represents the mass of gas produced using Grid V (standard), and M_i represents the mass of gas produced using Grid index, i.

Table 2 System properties, initial conditions, and pertinent model parameters

Parameter	Value				
Length (X)	150 m (75 m simulated)				
Width (Y)	150 m (75 m simulated)				
Depth (Z)	1 m				
Initial pressure (P)	7.59 MPa				
Initial temperature (T)	10.5 °C				
Case index	#1	#2	#3	#4	#5
Initial gas saturation in the system (Sg)	0.3	0.3	0.1	0.2	0.3
Initial water saturation in the system (Sw)	0.1	0.2	0.3	0.3	0.3
Initial hydrate saturation in the system (Sh)	0.6	0.5	0.6	0.5	0.4
Intrinsic permeability, <i>k</i>	$2.96 \times 10^{-14} \text{ m}^2$				
Specific heat capacity, <i>C_p</i>	1000 J/kg/°C				
Porosity, <i>φ</i>	0.3				
Salinity (<i>X_{iA}</i>)	3%				
Wet thermal conductivity (<i>k_{wet}</i>)	3.1 W/m/°C				
Sand thermal conductivity (<i>k_{dry}</i>)	0.5 W/m/°C				
Composite thermal conductivity (<i>k_Θ</i>)	$k_{\Theta} = k_{dry} + ((S_A)^{\frac{1}{2}} + (S_H)^{\frac{1}{2}})(k_{wet} - k_{dry}) + \phi S_I k_I$				
Relative permeability (<i>k_r</i>)	Modified stone's three phase method $k_{rA} = \max \left\{ 0, \min \left[\frac{S_A - S_{irA}}{S_A - S_{irA}}, 1 \right] \right\}$ $k_{rG} = \max \left\{ 0, \min \left[\frac{S_G - S_{irG}}{1 - S_{irG}}, 1 \right] \right\}$				
<i>n</i>	3				
<i>S_{irA}</i>	0.120				
<i>S_{irG}</i>	0.02				
Porous media module	EPM#1 (Evolving porous media)				
Capillary pressure model	Modified Brooks–Corey equation $P_{cap} = -F \cdot G \cdot P_{GE} (S^*)^v$, $S^* = \frac{S_A - S_{irA}}{1 - S_{irA}}$, $F = 1 + A \cdot Bx(a, b, SH)$				
Withdrawal rate, <i>W_R</i> (Depressurization)	0.01–0.6 kg/s				

In the modified Brooks–Corey equation, *P_{GE}* denotes gas entry pressure, *G* is the error function equation, *F* is the factor describing the effect of hydrate on capillary pressure. *A* is a parameter > 0, *Bx* is the incomplete beta function, and *a*, *b* are input arguments for *Bx*

As can be seen from Fig. 2, Grid 0 results in the under-prediction of the mass of methane produced from the reservoir. However, as Grid is refined with increasing Grid elements, it is noticed that results from the different Grids start converging to the same values. The resulting numerical error, *ε* keeps decreasing, and numerical predictions for Grid III, IV, and V yields the same cumulative production (overlapping) of methane at the end of 126 days. Since choosing a Grid with coarse discretization induces numerical errors, and too fine discretization increases computational cost. Therefore, Grid index III is chosen for conducting further simulations, as it provides both accuracy and optimum computational cost.

Concept of steady-state and phase equilibrium

The delineation of different causes of stopping of gas production requires application of concept of “phase equilibrium” and “steady-state.” These concepts are used in calculating and plotting “Contours of equilibrium pressure.” The three-phase equilibrium conditions (P–T) of methane gas hydrates for I–H–V and Lw–H–V were determined from the relationship described by Moridis et al. (2012). Equations 5 and 6 describe the relationship for I–H–V and Lw–H–V three-phase equilibrium conditions.

1. I–H–V (T < 273.2 K)

$$\ln(P_e) = -4.38921173434628 \times 10^1 + 7.76302133739303 \times 10^{-1}T - 7.27291427030502 \times 10^{-3}T^2 + 3.85413985900724 \times 10^{-5}T^3 - 1.03669656828834 \times 10^{-7}T^4 + 1.09882180475307 \times 10^{-10}T^5 \tag{5}$$

2. Lw–H–V (T > 273.2 K)

$$\ln(P_e) = -1.94138504464560 \times 10^5 + 3.31018213397926 \times 10^3T - 2.25540264493806 \times 10^1T^2 + 7.67559117787059 \times 10^{-2}T^3 - 1.30465829788791 \times 10^{-4}T^4 + 8.86065316687571 \times 10^{-8}T^5 \tag{6}$$

At the end of simulation, the above equations are used to calculate the equilibrium pressure (Pe). As described earlier, the contours of “pressure” and “equilibrium

Fig. 1 Illustration of Physical system with **a** Overall system with production well located at the center and **b** Neumann boundary conditions applied due to symmetry

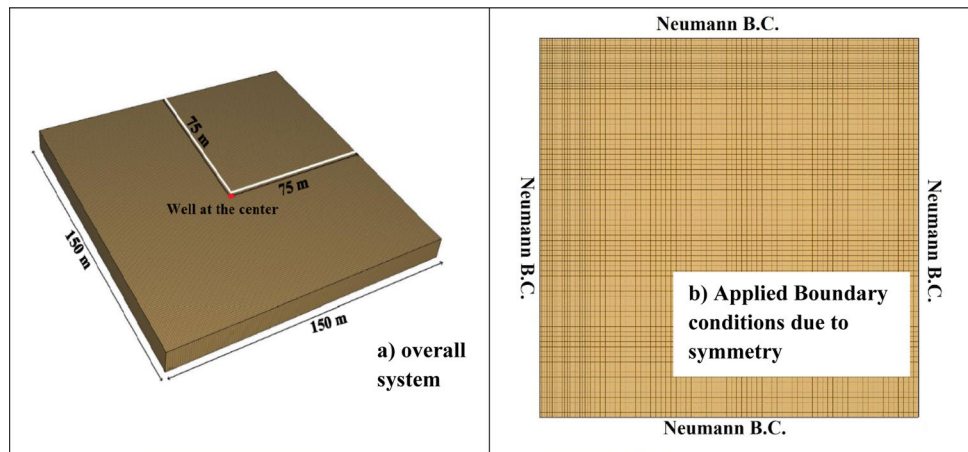


Table 3 Details of grid size and corresponding numerical error, ϵ

S. no.	Grid index	Number of elements	Numerical error, ϵ (%)
1	Grid 0	1699	7.2
2	Grid I	4324	4.0
3	Grid II	4999	1
4	Grid III	5724	0
5	Grid IV	15,724	0
6	Grid V	25,999	0

pressure” can be compared to establish whether or not the reservoir has achieved a steady-state or state of equilibrium. The identical distribution of pressure within the domain from the contours of pressure and equilibrium pressure indicates that the hydrate reservoir has reached a steady-state or state of equilibrium. On the contrary, a difference between the contour values of pressure and equilibrium pressure shows the existence of a driving force (ΔP). This also implies that the cause of stopping of gas production is likely due to some other reason such as ice formation or reformation of hydrates. Hence, other causes of stopping gas production must be investigated and confirmed from the saturation distribution of ice and hydrate.

Results and discussion

This section entails the results from the five different cases which are simulated. As described previously, based on the varying phase saturation of the hydrate reservoir, suitable depressurization conditions must be employed to maximize energy recovery through hydrate dissociation. As such, depressurization employs the technique of

withdrawing fluids from the well. This lowers the pressure and brings hydrate out of the stability zone. Therefore, this scenario requires using a particular withdrawal rate, which leads to cumulatively maximum and continuous gas production. Here, cumulative mass (kg) and volume (m^3) of methane produced from hydrate dissociation are reported. Moreover, the net mass of methane (including free gas) collected from the well is also reported. Also, to better understand the response of the system, contours of hydrate, ice, gas, water, pressure, and temperature are depicted for each case.

Variation of withdrawal rate and quantification of gas production

Case 1: $S_w = 0.1, S_g = 0.3$ & $S_h = 0.6$

In case 1, the reservoir is subjected to depressurization by the withdrawal of fluids from the well located at the center of the domain (See Fig. 1). Different withdrawal rates (W_R) ranging from 0.6 to 0.01 kg/s are applied to reduce the pressure and estimate the cumulative gas production behavior. Figure 3 (Left) shows a high value of $W_R = 0.6$ kg/s (not visible due to scale) leads to the rapid release of methane production. Since hydrate dissociation is endothermic, such a scenario leads to rapid cooling resulting in a temperature drop near the well. Similar behavior is observed for $W_R = 0.5, 0.4, 0.3, 0.1$ and 0.09 (kg/s). Further, as can be noted from Fig. 3. $W_R = 0.04$ kg/s yields a maximum cumulative production of 4.7×10^5 kg (From hydrate). Also, Fig. 3 (Right) depicts methane gas produced from hydrate dissociation (Both m^3 and kg), i.e., $7 \times 10^5 m^3$ and 4.7×10^5 kg. The overall gas produced at the well is found to be 7.7×10^5 kg.

Through Contours (Fig. 4a), it’s evident that for High $W_R = 0.6$ kg/s, we notice a large ΔP [$P_{eq} = 7.59$ MPa and $P_{min} = 1$ MPa] in the well vicinity, which causes rapid production but extends only up to 1.5 m. The temperature contour (Fig. 4b) shows a minimum $T = -15$ °C, which

is expected due to rapid depressurization, resulting in Ice formation shown in ice contour (See Fig. 4c). This restricts the flow of gas until it's completely stopped after just a runtime of 3.8 days. This indicates $W_R=0.6$ is an unfavorable rate for depressurization. Next, for a low $W_R=0.01$ (refer to Fig. 4i), pressure Contours show pressure drop, which extends well into the domain up to 50 m, but ΔP is very low [$P_{eq}=7.59$ MPa and $P_{min}=6.92$ MPa], which implies ineffective depressurization. The temperature conditions remain favorable, and no ice formation is noted. However, "Secondary hydrate" formation (See Fig. 4l) occurring near the well vicinity causes complete restriction of gas flow from the production well. Consequently, after 102 days, hydrate saturation drops to 0.5 from an initial value of 0.6, and gas production comes to a halt. For $W_R=0.04$ kg/s, we observe a much more desirable behavior through different contours. The pressure distribution can be seen to be extending up to

42 m. Moreover, a notable pressure drop is achieved with [$P_{eq}=7.59$ MPa and $P_{min}=2.75$ MPa]. Additionally, there is significant dissociation throughout the domain as pressure away from the well is reduced from 7.59 to 3.15 MPa. The temperature remains above 0 °C, and understandably, no ice formation is noted. However, after a production period of 345 days, the hydrate saturation drops from 0.6 to 0.46, and secondary hydrates appear near the well, which ultimately hinders the gas production in the well.

Case 2: $S_w=0.2, S_g=0.3$ & $S_h=0.5$

Case 2 is designed to understand the consequences of the increase in water saturation. As usual, different depressurization rates via withdrawal of fluids are applied. See Fig. 5 (Left) For higher withdrawal rates, in the range 0.6–0.2 kg/s; the gas production comes to a halt prematurely within 5 days. This occurs due to rapid cooling in the well vicinity, which causes decreased permeability due to ice formation. This decreased permeability chokes the gas production from the well. On the other hand, a much smaller magnitude of depressurization in the range of 0.01–0.04 kg/s leads to consistent gas production for up to 100 days. It is observed that increased withdrawal rates lead to a cumulatively higher quantity of methane production from the well. The maximum methane production is observed for $W_R=0.06$ kg/s. The net amount of methane produced from hydrate is found to be 7.42×10^5 m³ and 5.02×10^5 kg, respectively. In comparison to the previous case, a comparatively higher overall production at the well is found to be 8×10^5 kg.

Unlike case 1, where contours of temperature, pressure, hydrate, and ice saturation are shown, a more diverse strategy is employed to explain the system behavior for the different W_R range. For the higher depressurization scheme, $W_R=0.6$, P, T contours along with ice and relative permeability of Gas contours are depicted in Fig. 6. As can be noted for $W_R=0.6$, the pressure contours (See Fig. 6a) indicate that the system undergoes rapid depressurization. However, the pressure drop from $P_{eq}=7.59$ MPa to 1 MPa occurs

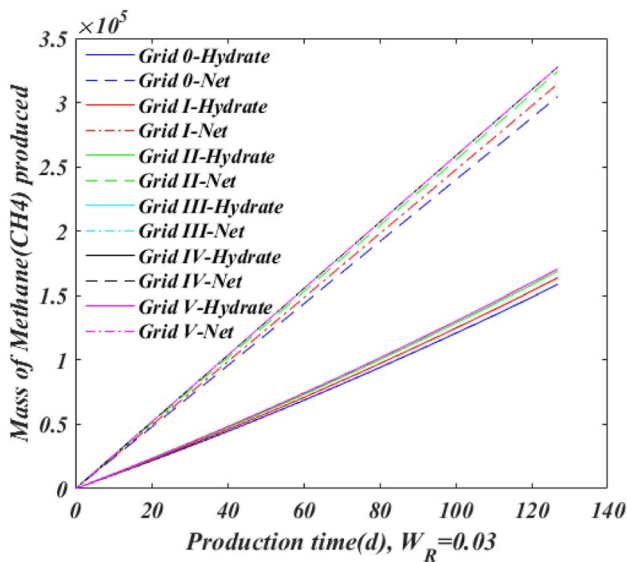
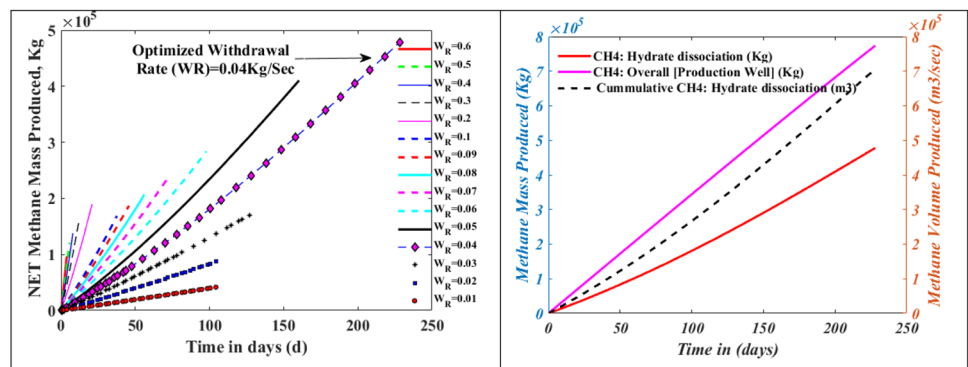


Fig. 2 Grid independence test depicting quantitative estimates for the different Grid index 0, I, II, III, IV and V

Fig. 3 (Left) Response to different depressurization rates for maximizing methane production. (Right) Net quantity of methane produced (m³/kg), overall and hydrate



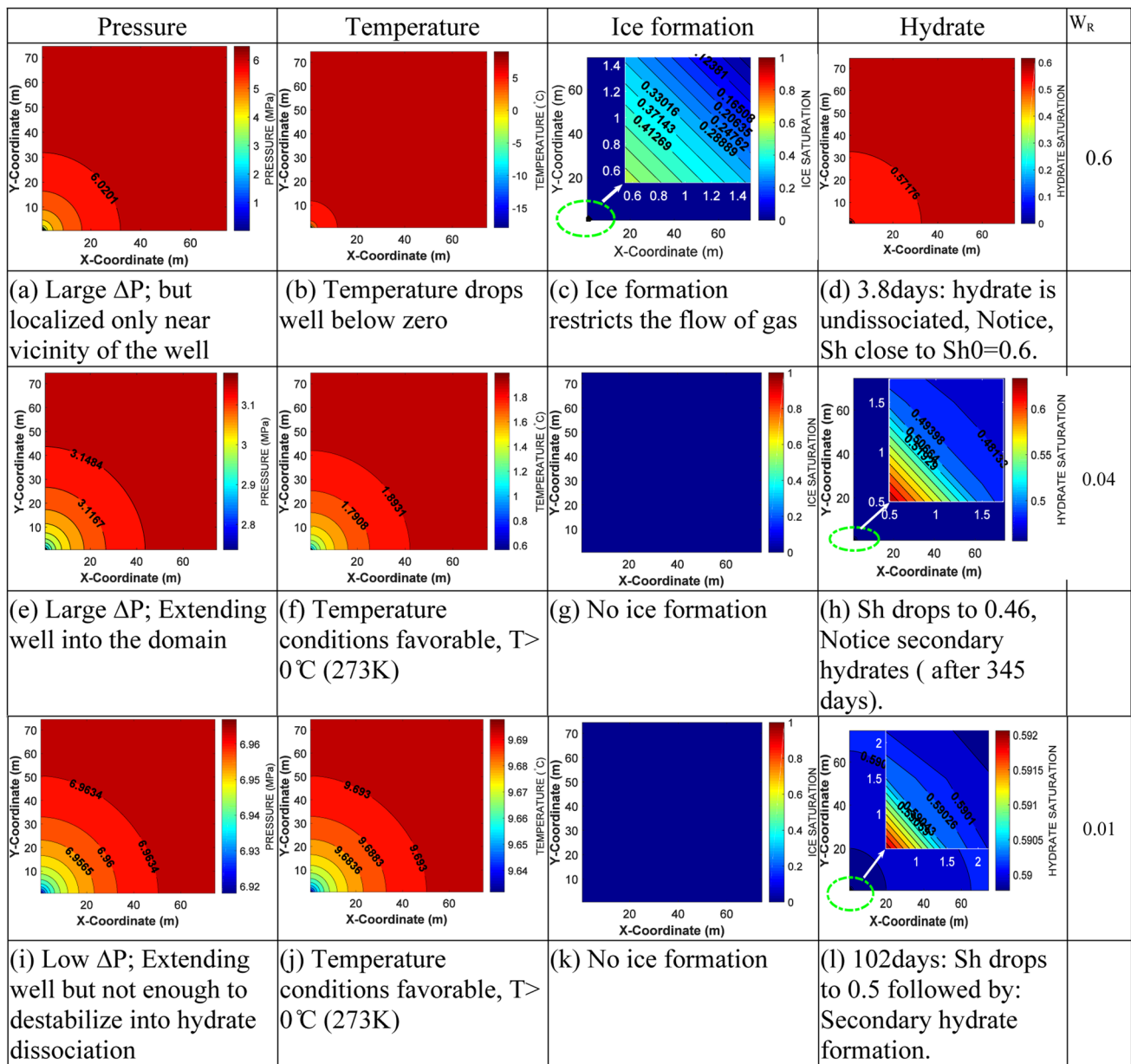


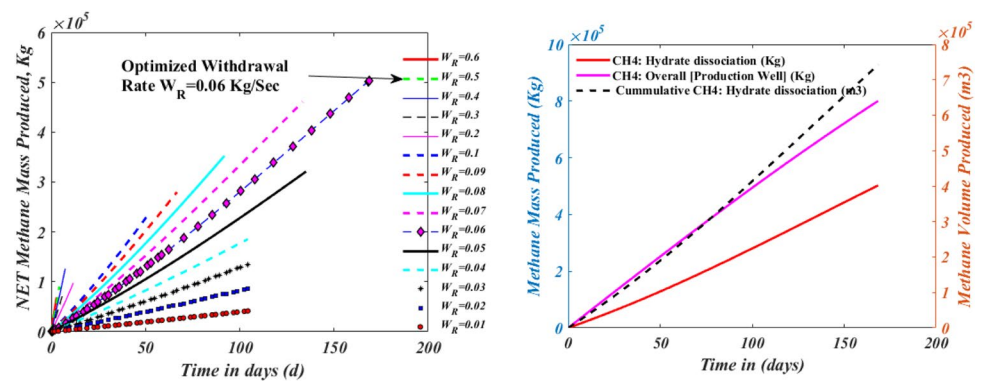
Fig. 4 Contour plots of thermodynamic parameters T, P, and saturation of ice and hydrates for inferring effectiveness of depressurization and cause of gas production stopping (Only extreme cases shown)

only in the vicinity of the well. Further, a pressure drop around 5 MPa is observed up to 5 m within the reservoir. This is relatively small, considering the fact that the domain extends up to 75 m in either direction (X and Y). Hence, it is inferred that this depressurization scheme induces dissociation, which is limited to a localized region. The temperature contours (See Fig. 6b) indicate that the temperature decreases to $-16^\circ C$, which leads to ice formation. From the ice contours (See Fig. 6c), a saturation of $S_{ICE}=0.7$ is observed near the well. This reduces the flow of gas, which is produced from hydrate dissociation. To provide a better

understanding and explanation, the relative permeability of gas contour is also shown in Fig. 6d. The relative permeability of gas indicates the ease with which the gas can move freely within the system. As marked by the levels, the contour indicates relative permeability drops from 0.22 at 1.4 m from the well to absolute 0 at the well. This is precisely why gas production stops for $W_R=0.6$ case.

For the $W_R=0.01$ case, the pressure contours (See Fig. 6i) show a much more extended depressurization behavior. A gradual pressure drop is observed throughout the domain. The pressure drops from $P_{eq}=7.59$ MPa

Fig. 5 (Left) Response to different depressurization rates for maximizing methane production. (Right) Net quantity of methane produced (m^3/kg), overall and hydrate



to 6.95 MPa from 0.5 to 75 m in both X and Y directions. The temperature contours (See Fig. 6j) show temperature, which is approximately $> 9^\circ\text{C}$, which alleviates any possibility of ice formation. Moreover, as shown in Fig. 5 (Left), continuous gas production is observed for approx. 100 days. Further, through the water contours, it is observed that water saturation (See Fig. 6j) increases from initial $Sw_0 = 0.2$ to $Sw > 0.21$ throughout the domain. This indicates that hydrate is dissociated throughout the domain rather than just being limited to the well vicinity. Further, the contours of hydrates (See Fig. 6l) indicate that maximum hydrate saturation occurs near the well region. This suggests that the reformation of hydrates occurs, which shows that the heat requirements are met through exothermic secondary hydrate formation. A further dissociation can be initiated through wellbore heating, which will melt the hydrates, and consequently, depressurization can be used. Coming to the maximum production case for $W_R = 0.06$ kg/s, the pressure contours (See Fig. 6e) show that a strong depressurization occurs throughout the domain. The maximum and minimum pressure within the domain is found to be 3.1 MPa and 2.7 MPa, respectively. This implies that pressure drops from an initial value of 7.59 MPa to roughly 3 MPa, which is appreciable. The temperature is found to be close to 0°C . However, $T > 0^\circ\text{C}$ is observed throughout the domain. The relative permeability of water is found to 0.1, which indicates that the movement of water is restricted and leads to “secondary hydrate formation.” The maximum saturation of hydrates, Sh , is found to 0.495 near the well. As compared to the initial value, a significant drop (0.6–0.35) in hydrate saturation is observed for $W_R = 0.06$, which shows that it’s the most suitable strategy and the best-case scenario for continuous production, i.e., 168 days.

Case 3: $Sw = 0.3$, $Sg = 0.1$ & $Sh = 0.6$

In case 3, a system with minimum gas saturation and 60% hydrate is simulated. Referring to Fig. 7, it is interesting to note that since the system contains a smaller quantity of free

gas, a clear trend can be observed from the (Left) plot in Fig. 7 depicting continuous cumulative production for different withdrawal rates. There is a clear demarcation from $W_R = 0.2$ to $W_R = 0.01$, which shows continuous production that lasts approximately 350 days. This behavior suggests that the present system containing a higher quantity of hydrate can be effectively depressurized with even a small driving force. Further, in the present case, $W_R = 0.08$ kg/s is found to yield a maximum quantity of gas production from the hydrate reservoir. Moreover, $W_R = 0.07$, 0.08, and 0.09 are found to produce approximately the same amount of gas. This behavior can be stated to be within the “maximum bracket.” As can be noted from Fig. 7 (Right), the net quantity of methane produced from hydrate dissociation is found to be 4.91×10^5 kg and 7.25×10^5 m^3 . The overall production is estimated at 5.5×10^5 kg.

For case 3, for better understanding, the reasons for stopping of gas production, the concept of equilibrium pressure contour is employed. This helps understand the behavior of the current system, which is mainly composed of hydrate and a relatively small quantity of free gas. As a result of depressurization, the free gas, along with gas produced from hydrate dissociation, is released. However, the main contribution comes from hydrate. Coming to a high depressurization case with $W_R = 0.6$, a high depressurization leads to fast dissociation. This results in the consumption of sensible heat from the surroundings of the well. Gas production lasts only 0.7 days. The cause of stopping of gas production is inferred from the Ice saturation and hydrate saturation contour. A remarkably cooled zone with a temperature of -4°C is seen from the temperature contours (See Fig. 8b). This zone extends from the well vicinity to approximately 2 m, and evidently, as can be noted from Fig. 8d (hydrate saturation), Sh becomes zero. On the other hand, the production of water within this zone leads to the formation of ice. This is shown in the ice contours (See Fig. 8c). Hence, it is inferred that for a system that is mainly composed of hydrate, $W_R = 0.6$ presents an unfavorable strategy for hydrate dissociation. For $W_R = 0.01$, as can be noticed from the pressure contours (See Fig. 8i), the pressure drops from initial $P_{eq} = 7.59$ MPa

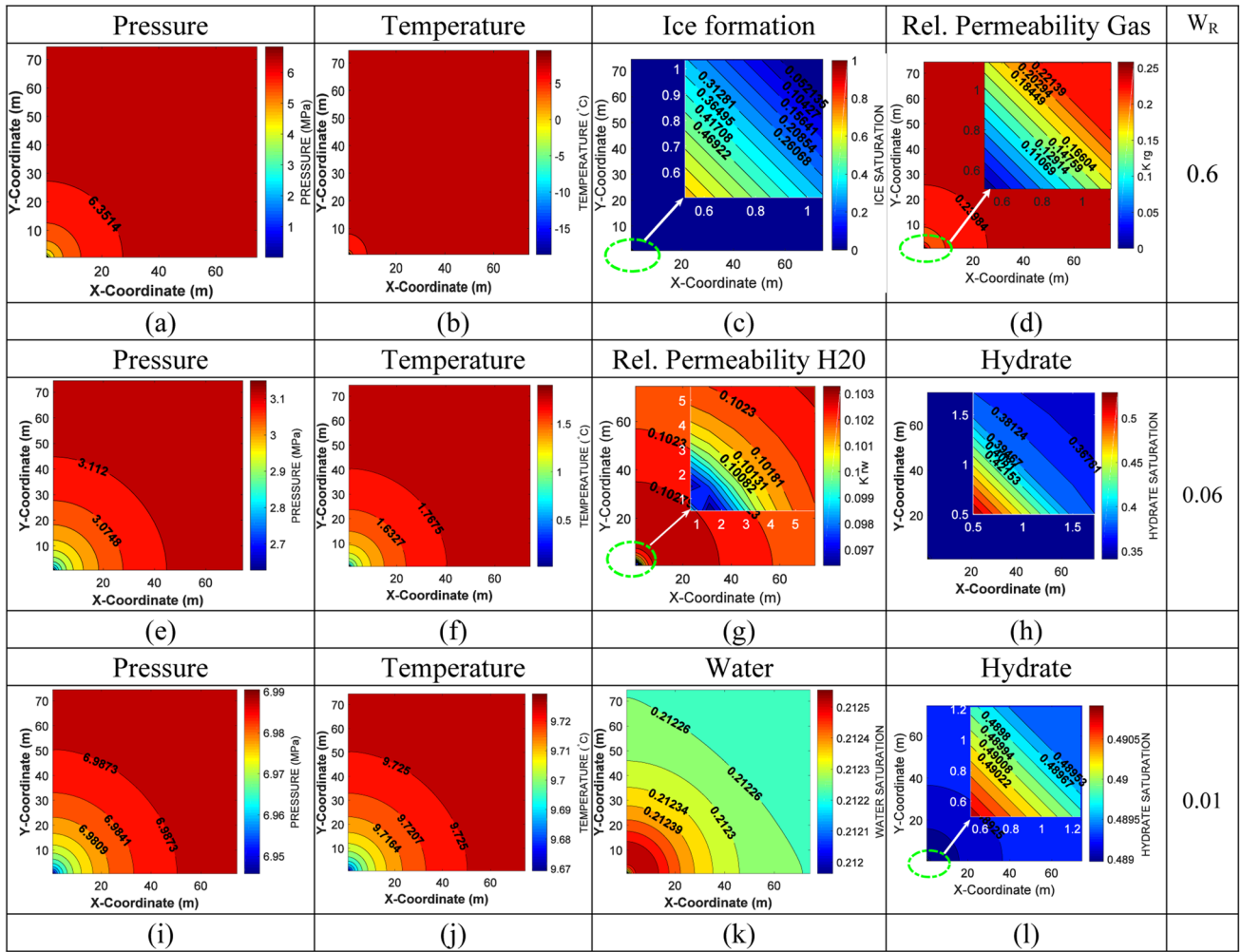
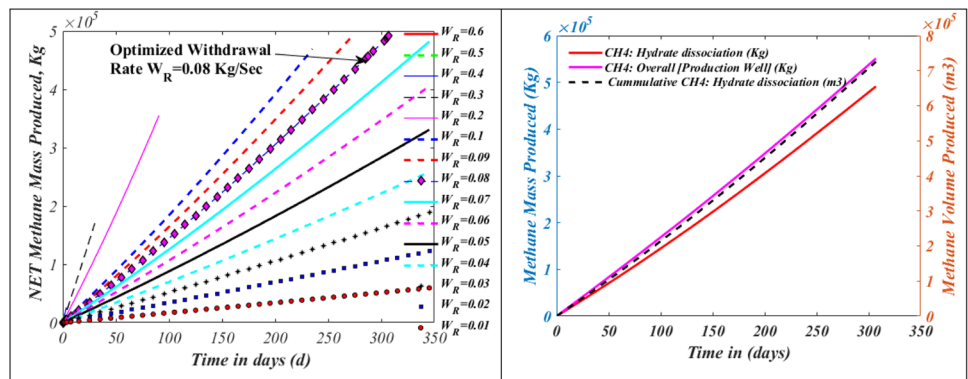


Fig. 6 Contour plots of thermodynamic parameters T, P, and saturation of ice and hydrates for inferring effectiveness of depressurization and cause of gas production stopping (Only extreme cases shown)

to 6.5 MPa. There is an extended pressure drop of 6.7 MPa up to 53 m from the well. The temperature contours (See Fig. 8j) indicate that the temperature remains sufficiently high, $T > 9\text{ }^\circ\text{C}$ (Therefore no ice formation). However, the cause of stopping of gas production is inferred from the

“equilibrium pressure contour.” If one takes a closer look, it can be noticed from Fig. 8i and k. (Case 0.01), both pressure and equilibrium pressure contours are exactly of the same distribution. This implies that the reservoir has reached a “steady-state.” The relative permeability of gas

Fig. 7 (Left) Response to different depressurization rates for maximizing methane production. (Right) Net quantity of methane produced (m^3/kg), overall and hydrate



is approximately of the order 10^{-2} , which indicates that gas movement within the reservoir is extremely limited. Hence, no further production.

For case $W_R=0.08$, an extended pressure drop from initial $P_{eq}=7.59$ MPa to 2.6 MPa is observed. The overall pressure in the entire domain is reduced to approximately 3.4 Mpa, which indicates that substantial dissociation takes place within the entire hydrate reservoir. The cause of gas production can be understood from the Equilibrium pressure Contours and hydrate saturation contours. As can be noticed from Fig. 8l, for case $W_R=0.01$, Sh drops to zero, and the equilibrium pressure contour is an exact match of pressure contour. This indicates that the system again reaches a steady-state, and methane gas production from the reservoir comes to an abrupt halt after 347 days.

Case 4: $S_w=0.3, S_g=0.2$ & $S_h=0.5$

In case 4, a system with 50% hydrate and appreciable quantities of water and free gas is simulated. As done previously, the variation of withdrawal-induced depressurization is performed. It is interesting to note that unlike previous cases, where a maximum production was associated with the maximum number of days, in this case, $W_R=0.05$ leads to continuous production for 313 days, and the maximum quantity of methane production is recorded (Refer to Fig. 9 Left). On the other hand, the withdrawal rate within a bracket of 0.04–0.01 gives continuous production for 347 days, which does not yield a maximum production output. For a higher rate of depressurization, i.e., in the range, 0.2–0.6 kg/s, a rapid production rate is observed. However, the production period is relatively small and lasts only up to 50 days (maximum). As can be noted from Fig. 9 (Right), for $W_R=0.05$, maximum cumulative methane production is found to be

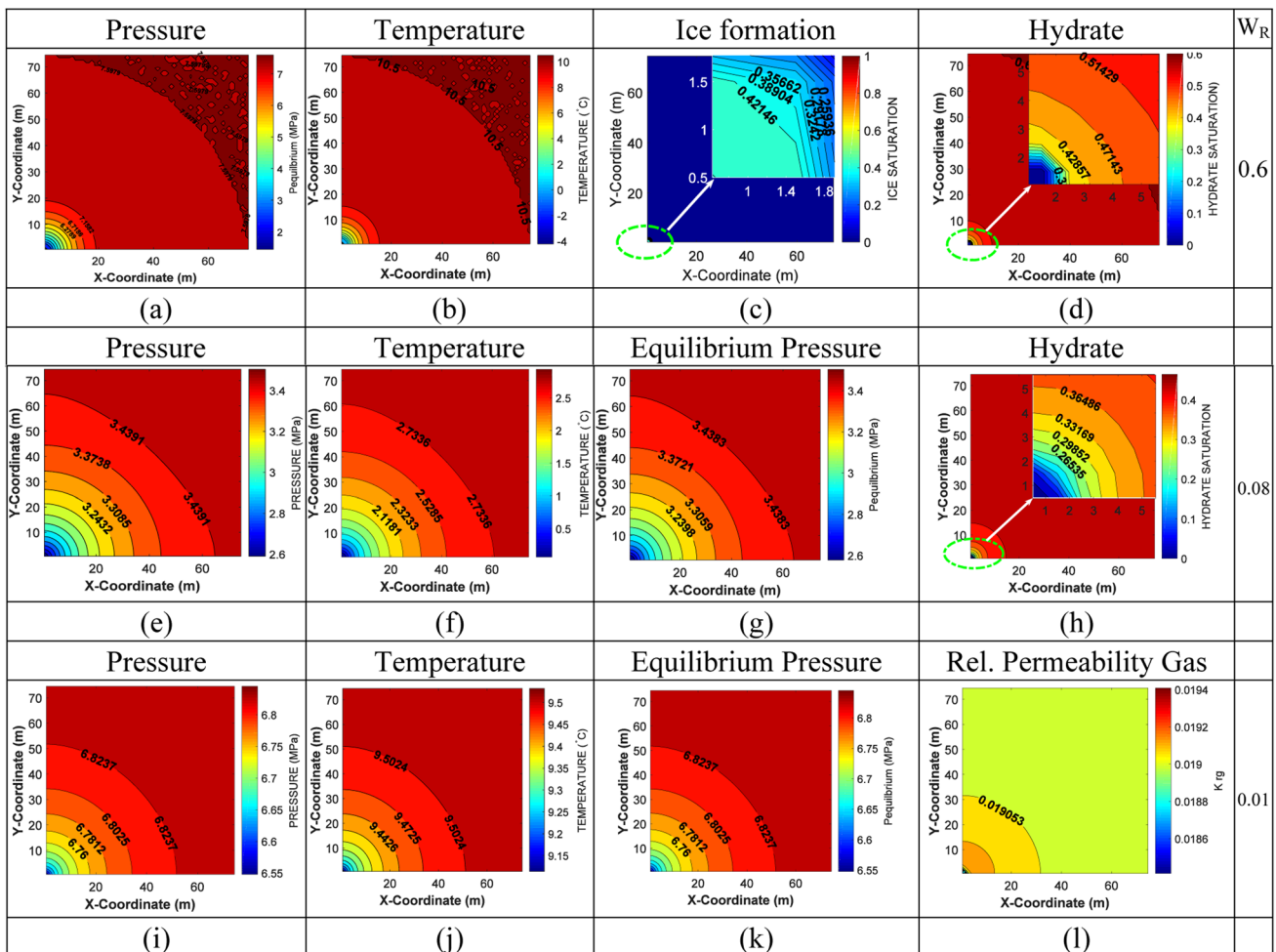


Fig. 8 Contour plots of thermodynamic parameters T, P, and saturation of ice and hydrates for inferring effectiveness of depressurization and cause of gas production stopping (Only extreme cases shown)

5.48×10^5 kg and 8.1×10^5 m³, respectively. The aggregate production at the well is found to be 7.41×10^5 kg.

In the previous cases, we have seen different causes that lead to the seizing of gas production from the well. This discussion is continued in this section. In the present case, Fig. 10 depicts the contours of three different depressurization rates, namely $W_R=0.6$, 0.05, and 0.01, respectively. For the high withdrawal rate, $W_R=0.6$, as can be noted from Fig. 10d, the hydrate saturation is reduced from 0.5 to zero in the well vicinity. This zone extends from the well to a distance of 1 m. From the ice saturation contours (See Fig. 10c), it can be seen that this zone is predominantly occupied by ice, which is formed due to the temperature dropping to 0 °C. a maximum ice saturation of 0.5 is observed in the well vicinity. This indicates that gas and water flow are severely restricted and progressively lead to stopping of gas production from the well. For $W_R=0.01$, the pressure and equilibrium pressure contours are plotted. Since the distribution of iso-pressure lines shows an exact replication, it can be concluded that the reservoir achieves a steady state after a period of 345 days. The temperature distribution is also shown (See Fig. 10j), which indicates that the temperature remains above 8 °C, and consequently ice formation problem is alleviated. Further, the relative gas permeability contours (See Fig. 10l) indicate that the gas flow is restricted (order of 10^{-2}), especially near the well, which is in harmony with previous contours. However, the significant contribution towards gas production comes from hydrate dissociation as an extended dissociation is observed throughout the domain with pressure dropping from P_{eq} value of 7.59–5.9 MPa.

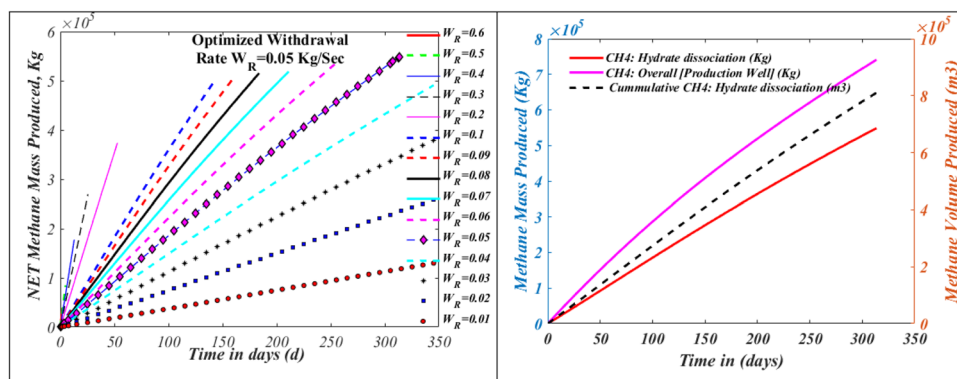
Coming to the maximum production scenario where depressurization with $W_R=0.05$ is carried out, the pressure contours (See Fig. 10e) indicate a favorable trend with progressive pressure drop throughout the domain. Near the well vicinity, a pressure drop from 7.59 MPa to 2.65 MPa is observed. Whereas, in the farther region of domain, a significant pressure drop from 7.59 to 3.05 MPa is noted. This implies that extended hydrate dissociation takes place and can be confirmed from hydrate saturation contour (See Fig. 10h), which shows

a significant saturation drop from 0.32 to 0.16. The temperature contours (See Fig. 10f) indicate that temperature remains 0.2 °C near the well vicinity, which implies that gas production is not restricted through the ice formation problem. Overall, the factors contributing to the drop in gas production and finally complete stopping of the gas release include the system reaching close to a steady-state and reduction of gas permeability, which impedes the gas migration to the well. A similar order of relative permeability as the previous case (i.e., 10^{-2}) is depicted in the relative permeability of gas contours (See Fig. 10g), which indicates weaker migration of released gas that eventually leads to the stopping of gas production.

Case 5: $S_w=0.3$, $S_g=0.3$ & $S_h=0.4$

In case 5, a system with 60% (water + free gas) and relatively small quantities of hydrate (40%) are simulated. Unlike previous examples, where the phase saturation of the system is more towards extrema, case 5 indicates a scenario that is more homogenous in different phase saturation. The system is subjected to depressurization with different magnitudes (0.6–0.01 kg/s) by the withdrawal of fluids from the well. As can be seen from Fig. 11, the maximum production range lies within the scope of $W_R=0.1$ –0.08 kg/s. In stark contrast to the previous case where continuous production is seen, increased sensitivity towards a particular depressurization range is seen due to the presence of free gas. For a low depressurization rate, $W_R=0.01$, we observe a continuous production that lasts around 70 days. Further increase in depressurization leads to increased cumulative production with a progressive increase in the production period. At the other extrema, depressurization within the range of 0.6–0.2 kg/s leads to a relatively small quantity of gas production that lasts < 10 days. The most suitable value for depressurization for this system is $WR=0.09$ kg/s, leading to continuous production for 130 days. The cumulative production for the maximum depressurization rate is shown in Fig. 11 (right). The aggregate mass and volume produced from hydrate dissociation are estimated to be 5.18×10^5 kg

Fig. 9 (Left) Response to different depressurization rates for maximizing methane production. (Right) Net quantity of methane produced (m³/kg), overall and hydrate



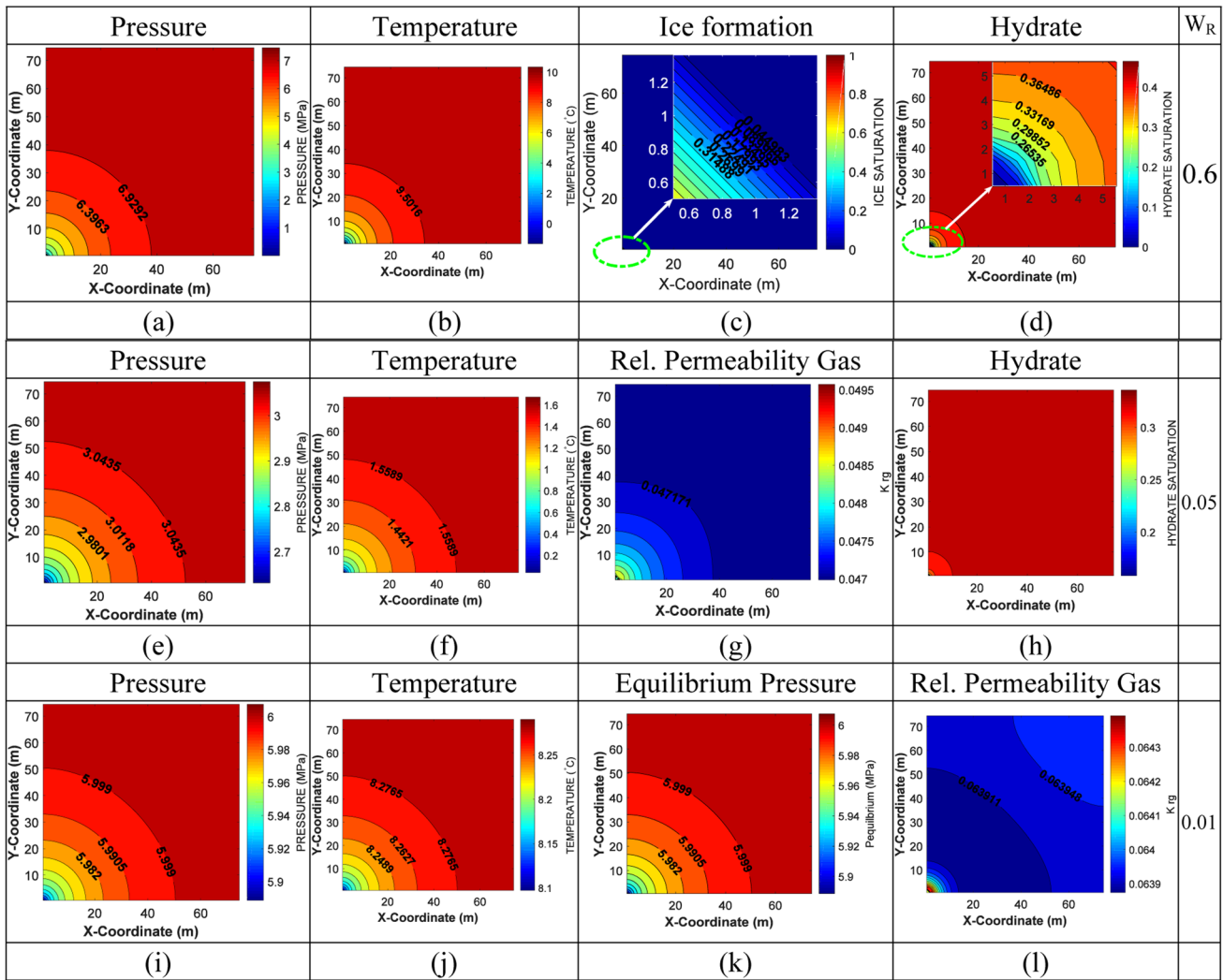


Fig. 10 Contour plots of thermodynamic parameters T, P, and saturation of ice and hydrates for inferring effectiveness of depressurization and cause of gas production stopping (Only extreme cases shown)

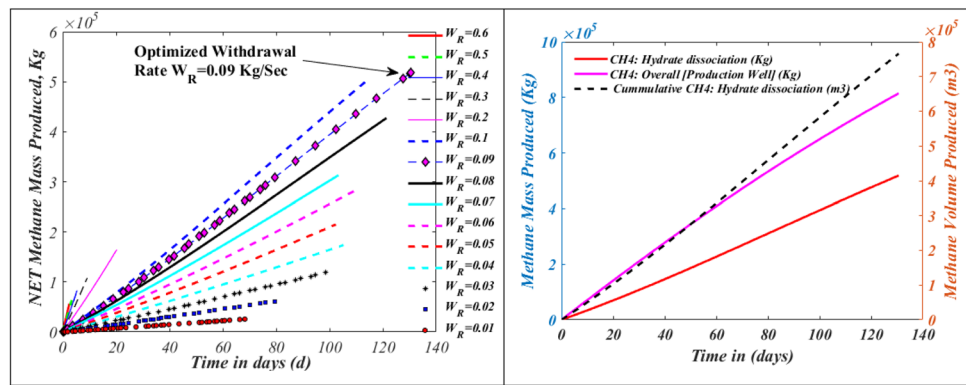
and $7.66 \times 10^5 \text{ m}^3$. The overall mass of methane produced at the well is estimated to be $8.14 \times 10^5 \text{ kg}$.

The contours in Fig. 12 indicate the scenario of thermodynamic P, T parameters along with saturation contours for ice and hydrate saturation. For $W_R = 0.6 \text{ kg/s}$, the pressure contours (See Fig. 12a) show that pressure reduces to 6 MPa from 7.59 MPa in the farther regions of the domain. Near the well vicinity, pressure decreases to 1 MPa, which implies strong depressurization. Consequently, with endothermic absorption of heat, the temperature drop in the region reaches $0 \text{ }^\circ\text{C}$, which is shown in ice contours (See Fig. 12b). Additionally, it's observed that hydrate saturation in the same zone reduces to zero. This implies that only gas, water, and ice coexist in the well vicinity. However, due to

the ice formation, gas seepage is constricted and eventually dies out. For $W_R = 0.01 \text{ kg/s}$, gas production remains stable and increases progressively for about 70 days. There is considerable hydrate dissociation throughout the hydrate zone. The confirmation is seen in pressure contours (See Fig. 12i), where pressure drops from 7.59 to 7.2 MPa. It is essential to notice that in this case, the conditions within the reservoir are favorable for gas migration. This conclusion can be inferred from the relative permeability of gas contours (See Fig. 12l), where the value of K_{rg} is 0.15.

Recall that in previous cases, K_{rg} was approximately of the order 10^{-2} . However, as can be noticed from the equilibrium pressure contours, the pressure distribution is an exact match of pressure contours (See Fig. 12i and

Fig. 11 (Left) Response to different depressurization rates for maximizing methane production. (Right) Net quantity of methane produced (m^3/kg), overall and hydrate



k). Since “equilibrium pressure” and “pressure” contours show the same distribution, it is inferred that the reservoirs reach a steady-state, and consequently, there is no further gas production. For the maximum production case with $W_R = 0.09$ kg/s, a substantial contribution of gas comes from hydrate dissociation as well. This is reflected in an extended pressure drop from an initial P_{eq} value of 7.59 MPa to an average value of 2.9 MPa. However, the temperature contours (See Fig. 12f) indicate that increasing hydrate dissociation leads to the temperature dropping to 0.2 °C near the well vicinity. The above explanation is confirmed from the water saturation contours (See Fig. 12g), which shows a significant increase from an initial SW_0 value of 0.3–0.45. The principal rationale for stopping gas production for the present scenario is inferred from hydrate saturation contours. As can be noted from the hydrate saturation contour (See Fig. 12h) there is an increased hydrate saturation from a value of 0.24–0.36, which indicates that initially, the hydrate saturation drops to 0.24 within the reservoir. Still, eventually, it increases to 0.36, which impedes the gas emancipation from the well. This leads to stopping of gas production after a continuous production period of 130 days.

The efficiency of gas production from hydrates

Figure 13 shows the dependency of withdrawal rate (0.01–0.6 kg/s) from the well on percentage conversion of hydrate to methane gas for different saturation cases of gas, water, and hydrate. For every case, the trend of percentage conversion of hydrate was not the same. The withdrawal rate leading to maximum gas production for all cases was found to be 0.04 kg/s (Case 1), 0.06 kg/s (Case 2), 0.08 kg/s (Case 3), 0.05 kg/s (Case 4) and 0.09 kg/s (Case 5) respectively.

For all cases, the percentage conversion of hydrate did not strictly follow an increasing or decreasing behavior with a change in withdrawal rate (Depressurization). Case 1 did not follow the increasing or decreasing behavior beyond the maximum withdrawal rate. For case 1, the maximum percentage conversion of hydrate is found to be 27% and

is attained at a withdrawal rate of 0.04 kg/s. There is an increase in percentage conversion of hydrate from a withdrawal rate of 0.01–0.04 kg/s. Further, a decrease in hydrate conversion percentage is observed for an increase in withdrawal rate from 0.04 to 0.6 kg/s, with an exception for $W_R = 0.2$ kg/s.

Similarly, for case 2, a maximum percentage conversion of hydrate is 34.5%, which is attained at a withdrawal rate of 0.06 kg/s. There is an increase in percentage conversion from the withdrawal rate of 0.01–0.06 kg/s. A decrease in hydrate conversion percent is observed from a withdrawal rate of 0.06–0.6 kg/s. The only exception being $W_R = 0.4$ kg/s, where the hydrate conversion percentage abruptly increases for withdrawal rate from 0.3 and 0.5 kg/s.

For case 3, a monotonous increase and decrease is observed from the maximum depressurization rate of 0.08 kg/s. A maximum of 28% hydrate conversion is observed for case 3. Also, unlike previous cases, it is observed that for a high withdrawal rate of 0.4, 0.5, and 0.6 kg/s, the hydrate conversion rate is almost negligible.

For cases 4 and 5, similar trends of increasing and decreasing hydrate dissociation are observed from the maximum depressurization rate. A maximum of 38% hydrate conversion is observed for case 4, while a much higher 45% hydrate conversion is observed for case 5. Moreover, for case 4, a broad distribution of withdrawal rate, which yields approximately more than 20% hydrate conversion, is observed for W_R values of 0.3–0.02 kg/s. This implies case 3 system is less sensitive towards the depressurization within this range. Although a particular withdrawal rate yields maximum gas production, there exists a broad range of depressurization, which yields continuous production. On the contrary, in case 5, there exists a sharp and distinct behavior in the consumption of hydrate among the different depressurization rates. This implies that the system is highly sensitive towards depressurization. There is a narrow range of 0.05–0.1, which yields continuous hydrate dissociation. The conversion efficiency within this range increases from a minimum of 20% to almost 45%. Hence such a system

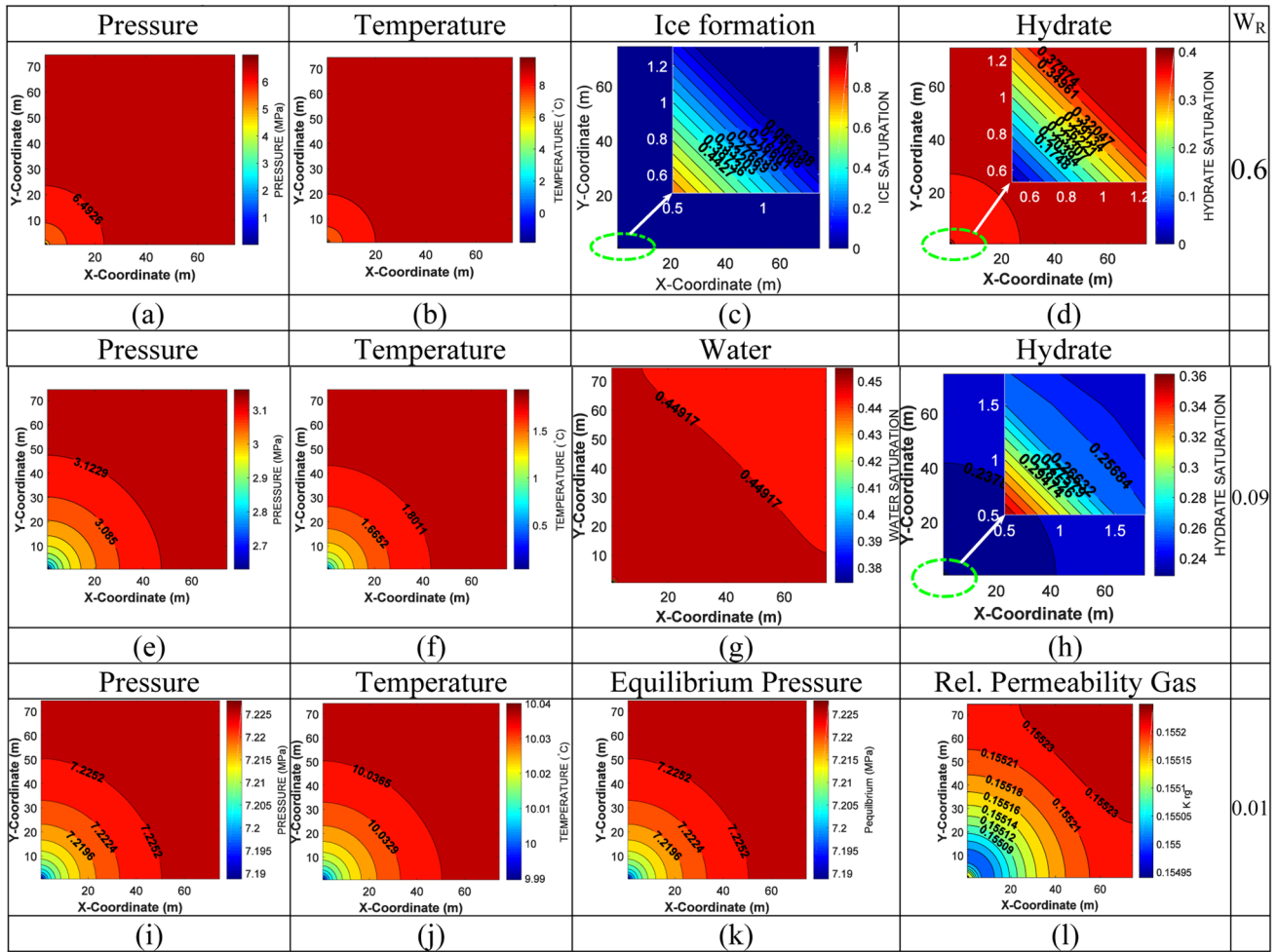


Fig. 12 Contour plots of thermodynamic parameters T, P, and saturation of ice and hydrates for inferring effectiveness of depressurization and cause of gas production stopping (Only extreme cases shown)

in case 5 showcases an urgent need towards application of suitable withdrawal rate to achieve maximum hydrate dissociation.

Overall, it is found that for the given system, i.e. fixed thermodynamic and lithological properties, depressurization rates below 0.1 kg/s are the most adequate and lead to cumulative maximum gas production. Moreover, ice production is the major cause of stopping of gas production for larger depressurization rates. Further, for systems with lower hydrate saturation, a stronger depressurization rate can be applied. This is due to the fact that amount of heat required for sustaining hydrate dissociation for such systems is considerably less. Hence, a smaller temperature drop occurs within such systems.

Conclusion

Based on the desired quantity of daily production (demand) and sustainable production for several years, a suitable depressurization rate must be determined. A sustainable production strategy also implies determining heating requirement, as well as different stages of well production, i.e. open end, flow period, injection etc. Therefore, to get a consistent amount of gas production, as well as knowing potential causes of stopping of production, predicting the response to depressurization is necessary. The present study investigated the gas production behavior through five different hydrate systems with varying phase saturation. The systems were subjected to a wide range of depressurization for the purpose of maximizing gas production and determination of sensitivity towards depressurization. The following conclusions are made concerning these systems.

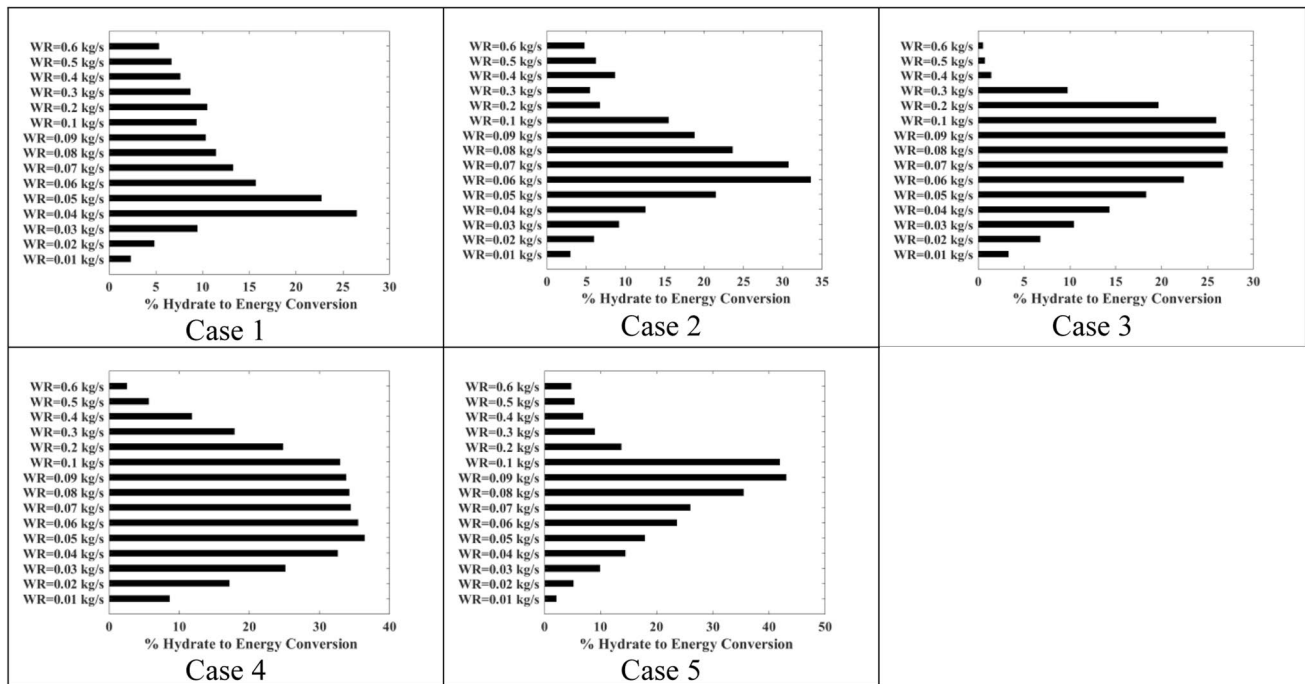


Fig. 13 Bar graphs depicting the percentage of hydrate dissociation for each case with different drawdown pressure

1. For the system with low gas saturation, i.e., case 3, the hydrate dissociation is susceptible to high depressurization rates and may lead to well choking. Hence, a low depressurization rate is recommended.
2. An increasing water and gas saturation makes hydrate depressurization more selective to dissociate hydrate effectively.
3. For systems with abundant free gas, initially, depressurization leads to the release of free gas. This is followed by actual depressurization of hydrate, and hence predicting depressurization response is necessary.
4. Different causes lead to the stopping of gas production from hydrate reservoirs. These include reduced relative permeability of gas within reservoirs in comparison to aqueous phase relative permeability.
5. Ice formation near the well vicinity is one of the major causes of stopping of gas production from the well.
6. Secondary hydrate formation near the well vicinity leads to restriction of gas flow and consequently causes stopping of gas production.
7. The hydrate reservoir can also reach a steady-state, which leads to the stopping of gas production after a consistent production period.

Funding The funding for this research work was provided by Gas hydrate research and technology centre (Grant No. ONG-1160-CHD).

References

- Arora A, Cameotra S (2014) Effects of biosurfactants on gas hydrates. *J Pet Environ Biotechnol*. <https://doi.org/10.4172/2157-7463.1000170>
- Arora A, Singh S (2015) Natural gas hydrate as an upcoming resource of energy. *J Pet Environ Biotechnol* 06:1–6. <https://doi.org/10.4172/2157-7463.1000199>
- Behresht J, Bryant SL (2012) Sedimentological control on saturation distribution in Arctic gas-hydrate-bearing sands. *Earth Planet Sci Lett* 341–344:114–127. <https://doi.org/10.1016/j.epsl.2012.06.019>
- Bhade P, Phirani J (2015) Gas production from layered methane hydrate reservoirs. *Energy* 82:686–696. <https://doi.org/10.1016/j.energy.2015.01.077>
- Birkedal KA, Freeman CM, Moridis GJ, Graue A (2014) Numerical predictions of experimentally observed methane hydrate dissociation and reformation in sandstone. *Energy Fuels* 28:5573–5586. <https://doi.org/10.1021/ef500255y>
- Bouriak S, Vanneste M, Saoutkine A (2000) Inferred gas hydrates and clay diapirs near the Storegga Slide on the southern edge of the Vøring Plateau, offshore Norway. *Mar Geol* 163:125–148. [https://doi.org/10.1016/S0025-3227\(99\)00115-2](https://doi.org/10.1016/S0025-3227(99)00115-2)
- Burwicz EB, Rüpke LH, Wallmann K (2011) Estimation of the global amount of submarine gas hydrates formed via microbial methane formation based on numerical reaction-transport modeling and a novel parameterization of Holocene sedimentation. *Geochim Cosmochim Acta* 75:4562–4576. <https://doi.org/10.1016/j.gca.2011.05.029>
- Chen L, Chi WC, Wu SK et al (2014) Two dimensional fluid flow models at two gas hydrate sites offshore southwestern Taiwan. *J Asian Earth Sci* 92:245–253. <https://doi.org/10.1016/j.jseaes.2014.01.004>
- Chong ZR, Yin Z, Linga P (2017) Production behavior from hydrate bearing marine sediments using depressurization approach.

- Energy Procedia 105:4963–4969. <https://doi.org/10.1016/j.egy-pro.2017.03.991>
- Circone S, Stern LA, Kirby SH et al (2000) Methane hydrate dissociation rates at 0.1 MPa and temperatures above 272 K. *Ann NY Acad Sci* 912:544–555. <https://doi.org/10.1111/j.1749-6632.2000.tb06809.x>
- Collett T (1995) Gas hydrate resources of the United States In: Gautier D, Dolton G (eds) *Natl. Assessment of US Oil & Gas Resources*, (CD-ROM) USGS Ser. 30, p 78 + CD
- Collett TS, Riedel M, Boswell R et al (2015) Indian National Gas Hydrate Program Expedition 01 report. *Sci Investig Rep*. <https://doi.org/10.3133/sir20125054>
- Crutchley GJ, Geiger S, Pecher IA et al (2010a) The potential influence of shallow gas and gas hydrates on sea floor erosion of Rock Garden, an uplifted ridge offshore of New Zealand. *Geo-Mar Lett* 30:283–303. <https://doi.org/10.1007/s00367-010-0186-y>
- Crutchley GJ, Pecher IA, Gorman AR et al (2010b) Seismic imaging of gas conduits beneath seafloor seep sites in a shallow marine gas hydrate province, Hikurangi Margin, New Zealand. *Mar Geol* 272:114–126. <https://doi.org/10.1016/j.margeo.2009.03.007>
- Crutchley GJ, Klaeschen D, Planert L et al (2014) The impact of fluid advection on gas hydrate stability: investigations at sites of methane seepage offshore Costa Rica. *Earth Planet Sci Lett* 401:95–109. <https://doi.org/10.1016/j.epsl.2014.05.045>
- Cui Y, Lu C, Wu M et al (2018) Review of exploration and production technology of natural gas hydrate. *Adv Geo-Energy Res* 2:53–62. <https://doi.org/10.26804/ager.2018.01.05>
- Davie MK, Buffett BA (2001) A numerical model for the formation of gas hydrate below the seafloor. *J Geophys Res Solid Earth* 106:497–514. <https://doi.org/10.1029/2000JB900363>
- Davie MK, Buffett BA (2003a) A steady state model for marine hydrate formation: constraints on methane supply from pore water sulfate profiles. *J Geophys Res Solid Earth*. <https://doi.org/10.1029/2002JB002300>
- Davie MK, Buffett BA (2003b) Sources of methane for marine gas hydrate: inferences from a comparison of observations and numerical models. *Earth Planet Sci Lett* 206:51–63. [https://doi.org/10.1016/S0012-821X\(02\)01064-6](https://doi.org/10.1016/S0012-821X(02)01064-6)
- De La Fuente M, Vaunat J, Marín-Moreno H (2019) Thermo-hydro-mechanical coupled modeling of methane hydrate-bearing sediments: formulation and application. *Energies*. <https://doi.org/10.3390/en12112178>
- Fang B, Ning F, Ou W et al (2019) The dynamic behavior of gas hydrate dissociation by heating in tight sandy reservoirs: a molecular dynamics simulation study. *Fuel*. <https://doi.org/10.1016/j.fuel.2019.116106>
- Feng JC, Wang Y, Sen LX et al (2015) Production behaviors and heat transfer characteristics of methane hydrate dissociation by depressurization in conjunction with warm water stimulation with dual horizontal wells. *Energy* 79:315–324. <https://doi.org/10.1016/j.energy.2014.11.018>
- Feng Y, Chen L, Suzuki A et al (2019) Enhancement of gas production from methane hydrate reservoirs by the combination of hydraulic fracturing and depressurization method. *Energy Convers Manag* 184:194–204. <https://doi.org/10.1016/j.enconman.2019.01.050>
- Field ME (1990) Submarine landslides associated with shallow seafloor gas and gas hydrates off northern California. In: *American Association of Petroleum Geologists Bulletin*. United States
- Frederick JM, Buffett BA (2011) Topography- and fracture-driven fluid focusing in layered oceanic sediments. *Geophys Res Lett*. <https://doi.org/10.1029/2010GL046027>
- Gao Yi, Yang M, Zheng JN, Chen B (2018) Production characteristics of two class water-excess methane hydrate deposits during depressurization. *Fuel* 232:99–107. <https://doi.org/10.1016/j.fuel.2018.05.137>
- Goto S, Yamano M, Morita S et al (2017) Physical and thermal properties of mud-dominant sediment from the Joetsu Basin in the eastern margin of the Japan Sea. *Mar Geophys Res* 38:393–407. <https://doi.org/10.1007/s11001-017-9302-y>
- Gupta A, Moridis GJ, Kneafsey TJ, Sloan ED (2009) Modeling pure methane hydrate dissociation using a numerical simulator from a novel combination of X-ray computed tomography and macroscopic data. *Energy Fuels* 23:5958–5965. <https://doi.org/10.1021/ef9006565>
- Heeschen KU, Abendroth S, Priegnitz M et al (2016) Gas production from methane hydrate: a laboratory simulation of the multistage depressurization test in Mallik, Northwest Territories, Canada. *Energy Fuels* 30:6210–6219. <https://doi.org/10.1021/acs.energyfuels.6b00297>
- Hillman JIT, Crutchley GJ, Kroeger KF (2020) Investigating the role of faults in fluid migration and gas hydrate formation along the southern Hikurangi Margin, New Zealand. *Mar Geophys Res* 41:1–19. <https://doi.org/10.1007/s11001-020-09400-2>
- Jin J, Wang X, He M et al (2020) Downward shift of gas hydrate stability zone due to seafloor erosion in the eastern Dongsha Island, South China Sea. *J Oceanol Limnol*. <https://doi.org/10.1007/s00343-020-0064-z>
- Khan SH, Misra AK, Majumder CB, Arora A (2020) Hydrate dissociation using microwaves, radio frequency, ultrasonic radiation, and plasma techniques. *ChemBioEng Rev* 7:130–146. <https://doi.org/10.1002/cben.202000004>
- Konno Y, Masuda Y, Hariguchi Y et al (2010) Key factors for depressurization-induced gas production from oceanic methane hydrates. *Energy Fuels* 24:1736–1744. <https://doi.org/10.1021/ef901115h>
- Konno Y, Masuda Y, Akamine K et al (2016) Sustainable gas production from methane hydrate reservoirs by the cyclic depressurization method. *Energy Convers Manag* 108:439–445. <https://doi.org/10.1016/j.enconman.2015.11.030>
- Kowalsky MB, Moridis GJ (2007) Comparison of kinetic and equilibrium reaction models in simulating gas hydrate behavior in porous media. *Energy Convers Manag* 48:1850–1863. <https://doi.org/10.1016/j.enconman.2007.01.017>
- Lee J, Ryu B-J, Yun T et al (2011) Review on the gas hydrate development and production as a new energy resource. *KSCIE J Civ Eng* 15:689–696. <https://doi.org/10.1007/s12205-011-0009-3>
- Li G, Moridis GJ, Zhang K, Li X (2011) The use of huff and puff method in a single horizontal well in gas production from marine gas hydrate deposits in the Shenhu Area of South China Sea. *J Pet Sci Eng* 77:49–68. <https://doi.org/10.1016/j.petrol.2011.02.009>
- Li XS, Yang B, Li G et al (2012a) Experimental study on gas production from methane hydrate in porous media by huff and puff method in pilot-scale hydrate simulator. *Fuel* 94:486–494. <https://doi.org/10.1016/j.fuel.2011.11.011>
- Li X-S, Yang B, Li G, Li B (2012b) Numerical simulation of gas production from natural gas hydrate using a single horizontal well by depressurization in Qilian Mountain Permafrost. *Ind Eng Chem Res* 51:4424–4432. <https://doi.org/10.1021/ie201940t>
- Li G, Li X-S, Yang B et al (2013) The use of dual horizontal wells in gas production from hydrate accumulations. *Appl Energy* 112:1303–1310. <https://doi.org/10.1016/j.apenergy.2013.03.057>
- Li B, Xu T, Zhang G et al (2018) An experimental study on gas production from fracture-filled hydrate by CO₂ and CO₂/N₂ replacement. *Energy Convers Manag* 165:738–747. <https://doi.org/10.1016/j.enconman.2018.03.095>
- Liang Y, Liu S, Zhao W et al (2018) Effects of vertical center well and side well on hydrate exploitation by depressurization and combination method with wellbore heating. *J Nat Gas Sci Eng* 55:154–164. <https://doi.org/10.1016/j.jngse.2018.04.030>
- Lu N, Hou J, Liu Y et al (2018) Stage analysis and production evaluation for class III gas hydrate deposit by depressurization. *Energy* 165:501–511. <https://doi.org/10.1016/j.energy.2018.09.184>

- Majorowicz J, Osadetz K (2001) Gas hydrate distribution and volume in Canada. *Am Assoc Pet Geol Bull.* <https://doi.org/10.1306/8626CA9B-173B-11D7-8645000102C1865D>
- Malinverno A (2010) Marine gas hydrates in thin sand layers that soak up microbial methane. *Earth Planet Sci Lett* 292:399–408. <https://doi.org/10.1016/j.epsl.2010.02.008>
- Malinverno A, Goldberg DS (2015) Testing short-range migration of microbial methane as a hydrate formation mechanism: results from Andaman Sea and Kumano Basin drill sites and global implications. *Earth Planet Sci Lett* 422:105–114. <https://doi.org/10.1016/j.epsl.2015.04.019>
- Marin-Moreno H (2014) Numerical modelling of overpressure generation in deep basins and response of Arctic gas hydrate to ocean warming. University of Southampton
- Moridis G, Sloan E (2007) Gas production potential of disperse low-saturation hydrate accumulations in oceanic sediments. *Energy Convers Manag* 48:1834–1849. <https://doi.org/10.1016/j.enconman.2007.01.023>
- Moridis G, Reagan M (2007) Strategies for Gas Production From Oceanic Class 3 Hydrate Accumulations. offshore Technol Conf. <https://doi.org/10.4043/18865-MS>
- Moridis GJ, Kowalsky MB, Karsten P (2005) HYDRATERESSIM User's Manual: a numerical simulator for modeling the behavior of hydrates in geologic media
- Moridis GJ, Kowalsky MB, Karsten P (2012) TOUGH+HYDRATE v1.2 User's Manual: a code for the simulation of system behavior in hydrate-bearing geologic media. Berkeley, California
- Moridis GJ, Reagan MT, Queiruga AF (2019) Gas Hydrate Production Testing: Design Process and Modeling Results. Offshore Technol Conf 15. <https://doi.org/10.4043/29432-MS>
- Nixon M, Hayley J (2011) Submarine slope failure due to gas hydrate dissociation: a preliminary quantification. *Can Geotech J* 44:314–325. <https://doi.org/10.1139/t06-121>
- Nole M, Daigle H, Cook AE, Malinverno A (2016) Short-range, overpressure-driven methane migration in coarse-grained gas hydrate reservoirs. *Geophys Res Lett* 43:9500–9508. <https://doi.org/10.1002/2016GL070096>
- Nole M, Daigle H, Cook AE et al (2017) Linking basin-scale and pore-scale gas hydrate distribution patterns in diffusion-dominated marine hydrate systems. *Geochem Geophys Geosyst* 18:653–675. <https://doi.org/10.1002/2016GC006662>
- Nole M, Daigle H, Cook AE et al (2018) Burial-driven methane recycling in marine gas hydrate systems. *Earth Planet Sci Lett* 499:197–204. <https://doi.org/10.1016/j.epsl.2018.07.036>
- Oliveira S, Vilhena O, da Costa E (2010) Time–frequency spectral signature of Pelotas Basin deep water gas hydrates system. *Mar Geophys Res* 31:89–97. <https://doi.org/10.1007/s11001-010-9085-x>
- Phirani J, Mohanty KK, Hirasaki GJ (2009) Warm water flooding of unconfined gas hydrate reservoirs. *Energy Fuels* 23:4507–4514. <https://doi.org/10.1021/ef900291j>
- Riley D, Marin-Moreno H, Minshull TA (2019) The effect of heterogeneities in hydrate saturation on gas production from natural systems. *J Pet Sci Eng* 183:106452. <https://doi.org/10.1016/j.petrol.2019.106452>
- Riley D, Schaafsma M, Marin-Moreno H, Minshull TA (2020) A social, environmental and economic evaluation protocol for potential gas hydrate exploitation projects. *Appl Energy* 263:114651. <https://doi.org/10.1016/j.apenergy.2020.114651>
- Ruan X, Song Y, Zhao J et al (2012) Numerical simulation of methane production from hydrates induced by different depressurizing approaches. *Energies* 5:438–458. <https://doi.org/10.3390/en5020438>
- Seol Y, Myshakin E (2011) Experimental and numerical observations of hydrate reformation during depressurization in a core-scale reactor. *Energy Fuels* 25:1099–1110. <https://doi.org/10.1021/ef1014567>
- Shelander D, Dai J, Bunge G (2010) Predicting saturation of gas hydrates using pre-stack seismic data, Gulf of Mexico. *Mar Geophys Res* 31:39–57. <https://doi.org/10.1007/s11001-010-9087-8>
- Singh S, Balomajumder C, Arora A (2015) Natural gas hydrate (clathrates) as an untapped resource of natural gas. *J Pet Environ Biotechnol* 06:4–6. <https://doi.org/10.4172/2157-7463.1000234>
- Sloan ED, Koh CA (2007) Clathrate hydrates of natural gases, 3rd edn. CRC Press, Boca Raton
- Song Y, Cheng C, Zhao J et al (2015) Evaluation of gas production from methane hydrates using depressurization, thermal stimulation and combined methods. *Appl Energy* 145:265–277. <https://doi.org/10.1016/j.apenergy.2015.02.040>
- Su Z, Moridis GJ, Zhang K, Wu N (2012) A huff-and-puff production of gas hydrate deposits in Shenhu area of South China Sea through a vertical well. *J Pet Sci Eng* 86–87:54–61. <https://doi.org/10.1016/j.petrol.2012.03.020>
- Sun R, Fan Z, Yang M et al (2019) Experimental investigation into the dissociation of methane hydrate near ice-freezing point induced by depressurization and the concomitant metastable phases. *J Nat Gas Sci Eng* 65:125–134. <https://doi.org/10.1016/j.jngse.2019.03.001>
- Tang LG, Sen LX, Feng ZP et al (2007) Control mechanisms for gas hydrate production by depressurization in different scale hydrate reservoirs. *Energy Fuels* 21:227–233. <https://doi.org/10.1021/ef0601869>
- Teng Y, Zhang D (2020) Comprehensive study and comparison of equilibrium and kinetic models in simulation of hydrate reaction in porous media. *J Comput Phys* 404:13298. <https://doi.org/10.1016/j.jcp.2019.109094>
- Terzariol M, Goldshtein G, Santamarina JC (2017) Maximum recoverable gas from hydrate bearing sediments by depressurization. *Energy* 141:1622–1628. <https://doi.org/10.1016/j.energy.2017.11.076>
- VanderBeek BP, Rempel AW (2018) On the importance of advective versus diffusive transport in controlling the distribution of methane hydrate in heterogeneous marine sediments. *J Geophys Res Solid Earth* 123:5394–5411. <https://doi.org/10.1029/2017JB015298>
- Waite WF, Ruppel CD, Boze L-G, Lorenson TD, Buczkowski BJ, McMullen KY, Kvenvolden KA (2020) Preliminary global database of known and inferred gas hydrate locations [Data set]. U.S. Geological Survey. <https://doi.org/10.5066/P9LLFVJM>
- Wan Y, Wu N, Hu G et al (2018) Reservoir stability in the process of natural gas hydrate production by depressurization in the shenhu area of the south China sea. *Nat Gas Ind B* 5:631–643. <https://doi.org/10.1016/j.ngib.2018.11.012>
- Wang J, Wu S, Geng J, Jaiswal P (2018) Acoustic wave attenuation in the gas hydrate-bearing sediments of Well GC955H, Gulf of Mexico. *Mar Geophys Res* 39:509–522. <https://doi.org/10.1007/s11001-017-9336-1>
- Wilder JW, Moridis GJ, Wilson SJ, Kurihara M, White MD, Masuda Y, Anderson BJ, Collett TS, Hunter RB, Narita H, Pooladi-Darvish M, Rose K, Boswell R (2008) An international effort to compare gas hydrate reservoir simulators. In: Englezos P, Ripmeester J (eds) Proceedings of the 6th International Conference on Gas Hydrates, Vancouver, Canada, p 12. Paper 5727
- Xu CG, Cai J, Yu YS et al (2018) Research on micro-mechanism and efficiency of CH₄ exploitation via CH₄-CO₂ replacement from natural gas hydrates. *Fuel* 216:255–265. <https://doi.org/10.1016/j.fuel.2017.12.022>
- Yan C, Li Y, Cheng Y et al (2018) Sand production evaluation during gas production from natural gas hydrates. *J Nat Gas Sci Eng* 57:77–88. <https://doi.org/10.1016/j.jngse.2018.07.006>

- Yang X, Sun CY, Su KH et al (2012) A three-dimensional study on the formation and dissociation of methane hydrate in porous sediment by depressurization. *Energy Convers Manag* 56:1–7. <https://doi.org/10.1016/j.enconman.2011.11.006>
- Yang R, Su M, Qiao S et al (2015) Migration of methane associated with gas hydrates of the Shenhu Area, northern slope of South China Sea. *Mar Geophys Res* 36:253–261. <https://doi.org/10.1007/s11001-015-9249-9>
- Yi BY, Lee GH, Kang NK et al (2018) Deterministic estimation of gas-hydrate resource volume in a small area of the Ulleung Basin, East Sea (Japan Sea) from rock physics modeling and pre-stack inversion. *Mar Pet Geol* 92:597–608. <https://doi.org/10.1016/j.marpetgeo.2017.11.023>
- Yin Z, Chong ZR, Tan HK, Linga P (2016) Review of gas hydrate dissociation kinetic models for energy recovery. *J Nat Gas Sci Eng* 35:1362–1387. <https://doi.org/10.1016/j.jngse.2016.04.050>
- You K, Flemings PB (2018) Methane hydrate formation in thick sandstones by free gas flow. *J Geophys Res Solid Earth* 123:4582–4600. <https://doi.org/10.1029/2018JB015683>
- You K, DiCarlo D, Flemings PB (2015) Quantifying hydrate solidification front advancing using method of characteristics. *J Geophys Res Solid Earth* 120:6681–6697. <https://doi.org/10.1002/2015JB011985>
- Yu T, Guan G, Abudula A et al (2019) Gas recovery enhancement from methane hydrate reservoir in the Nankai Trough using vertical wells. *Energy* 166:834–844. <https://doi.org/10.1016/j.energy.2018.10.155>
- Yu T, Guan G, Abudula A, Wang D (2020) 3D investigation of the effects of multiple-well systems on methane hydrate production in a low-permeability reservoir. *J Nat Gas Sci Eng* 76:103213. <https://doi.org/10.1016/j.jngse.2020.103213>
- Yuan Y, Xu T, Xin X, Xia Y (2017) Multiphase flow behavior of layered methane hydrate reservoir induced by gas production. *Geofluids*. <https://doi.org/10.1155/2017/7851031>
- Zhou M, Soga K, Xu E et al (2014) Numerical study on Eastern Nankai Trough gas hydrate production test. *Proc Annu Offshore Technol Conf* 2:996–1014. <https://doi.org/10.4043/25169-ms>

Publisher's Note Springer Nature remains neutral with regard to jurisdictional claims in published maps and institutional affiliations.